The Interaction of Simulated Squall Lines with Idealized Mountain Ridges

JEFFREY FRAME AND PAUL MARKOWSKI

Department of Meteorology, The Pennsylvania State University, University Park, Pennsylvania

(Manuscript received 22 December 2004, in final form 14 October 2005)

ABSTRACT

Numerical simulations of squall lines traversing sinusoidal mountain ridges are performed using the Advanced Regional Prediction System cloud-resolving model. Precipitation and updraft strength are enhanced through orographic ascent as a squall line approaches a ridge. The simulated squall line then weakens as it descends the ridge because some of the cold pool is blocked by the terrain, resulting in less lift along the gust front and weaker convective cells. The flow within the cold pool accelerates slightly and the depth of the cold air decreases owing to upstream blocking, transitioning the flow in the cold pool head from subcritical to supercritical, then back to subcritical at the bottom of the ridge. A hydraulic jump forms when the flow transitions the second time, enabling the development of a new convective line downwind of the mountain. These new updrafts grow and eventually replace the older updrafts that weakened during descent. This process results in the discrete propagation of a squall line just downstream of a ridge, resulting in the formation of rain shadows downstream from topographic features. Discrete propagation only occurs if a ridge is of sufficient height, however. This replacement process repeats itself if a squall line encounters multiple ridges. The risk of damaging winds from a squall line is greater on the lee side of ridges and on the top of high ridges. These terrain-forced intensity fluctuations increase with mountain height, because the higher terrain permits even less cold air to flow over it. A wider ridge results in a more gradual orographic enhancement and downslope-induced weakening.

1. Introduction

Squall lines have been among the most intensely studied convective phenomena, in both observations (e.g., Newton 1950; Smull and Houze 1985; Braun and Houze 1994) and numerical simulations (e.g., Moncrieff and Miller 1976; Rotunno et al. 1988; Yang and Houze 1995; Coniglio and Stensrud 2001). The recent simulations of Fovell and Tan (1998), Lin et al. (1998), and Lin and Joyce (2001) focus on the life cycles of the convective elements that compose a squall line. These studies support the long-standing notion (Newton 1950) that new convective cells are initiated by the dynamically forced low-level updraft at the gust front (i.e., the gust front updraft or GFU). These updrafts subsequently deepen, intensify, and eventually separate themselves from the GFU. After the cells reach maturity, they eventually decay as they move farther away from the potentially warm environmental inflow and as their supply of buoyant air becomes eroded through mixing. Many simulations reveal three or more active cells within a line-normal cross section. For a lengthy review of squall-line morphology and dynamics, the reader is referred to the summary presented by Houze (2004).

The purpose of a majority of previous squall-line simulation studies has been to investigate squall-line dynamics. Thus, it was important that the squall lines were free of outside influences, such as topography. Squall lines, however, are not limited to regions with negligible topographic relief. For example, the terrain in parts of the eastern United States is characterized by the ridges and valleys of the Appalachian Mountains. These same areas also are frequented by squall lines, most commonly in advance of warm season cold fronts. Squall lines are also known to occur in other parts of the world characterized by complex terrain.

A review of the literature reveals that relatively little work has been done on the interaction between deep, moist convection and terrain. There have been several studies on initiation of convection by terrain (e.g., Raymond and Wilkening 1980; Karyampudi et al. 1995; Grady and Verlinde 1997). Our focus, however, is on

Corresponding author address: Jeffrey W. Frame, Dept. of Meteorology, The Pennsylvania State University, 503 Walker Bldg., University Park, PA 16802.
E-mail: jwf155@psu.edu

the interaction between preexisting squall lines and idealized terrain. Specifically, we are concerned with how terrain features, specifically mountain ridges, affect squall-line evolution.

One previous study (Teng et al. 2000) documented an interaction between a squall line and the Central Mountain Range on the island of Taiwan during the Taiwan Area Mesoscale Experiment (Kuo and Chen 1990). The Central Mountain Range is about 100 km across and has peaks over 4000 m high. The squall line moved from the Taiwan Strait into the mountainous areas of Taiwan and then dissipated. The terrain retarded the speed of the gust front, thereby forcing the orientation of the squall line to become parallel to the terrain. The higher levels of the system, however, were not slowed by the terrain. This differential acceleration with height disrupted the upshear tilt of the updrafts, and allowed precipitation to fall back into them. Additionally, the rear-to-front (RTF) flow (Smull and Houze 1987; Weisman 1992) was subjected to orographic lifting and became ingested into the updrafts. Thus, the squall line dissipated because it was deprived of conditionally unstable inflow.

Although additional observations of squall-line interactions with terrain will be important in advancing our understanding of how terrain can alter convection, a numerical model allows for the effects of terrain to be isolated from the internal dynamics of the convection. The purpose of this paper is to explore the effects of idealized mountain ridges, having a variety of geometries, on a mature squall line. A description of the model parameters and experimental design is found in section 2. The results of the control simulations are found in section 3 and the mountain ridge simulations are presented in section 4. A summary of the results is found in section 5.

2. Methodology

a. Model specifications

The Advanced Regional Prediction System (ARPS) model, version 4.5.2 (Xue et al. 2000, 2001), is employed for all of the simulations. The model grid is 400 km in the cross-line direction x, 60 km in the along-line direction y, and 17 km in the vertical direction z. Open radiation boundary conditions are imposed at the eastern and western boundaries of the domain as described in Klemp and Wilhelmson (1978). Periodic boundary conditions are used on the northern and southern boundaries of the domain. This means that there are no line-end effects, such as bookend vortices (Weisman 1993) and that the domain can be a relatively short 60 km in the along-line direction, as in Bryan et al. (2003).

The simulations employ a horizontal grid spacing of 1.25 km. This is coarser than the 100-m grid spacing advocated by Bryan et al. (2003) for simulations of deep moist convection. A grid spacing on the order of 1 km is able to reproduce the basic squall-line structure and circulation (Bryan et al. 2003). Also, it is not yet computationally practical to investigate such a large parameter space on a grid as extensive as this study requires using 100-m grid spacing, especially with no grid translation. Furthermore, it is well known (e.g., Adlerman and Droegemeier 2002) that simulations of convective storms are sensitive not only to the grid resolution employed, but to other model parameterizations as well. We feel that sacrificing the parameter space for high resolution is not practical for a pilot study such as this, especially when other model schemes can influence the results in a manner similar to the grid resolution. The vertical grid is a stretched terrain-following grid with an average spacing of 500 m and a minimum spacing of 150 m near the surface. A rigid lid exists at the top of the domain, with a 5-km-deep sponge layer beneath it to absorb vertically propagating gravity waves.

The prestorm environment is horizontally homogeneous, with a surface temperature of 300 K and a surface mixing ratio of 14 g kg^{-1}. The vertical thermodynamic profile (Fig. 1; Weisman and Klemp 1982) contains approximately 2200 J kg^{-1} of convective available potential energy and very little convective inhibition. The vertical wind profile consists of low-level westerly shear, with the zonal wind speed increasing linearly from zero at the surface to 17.5 m s^{-1} at an altitude of 2500 m. The wind velocity is constant with height above 2500 m. This magnitude of shear falls within the optimal range that maximizes squall-line intensity and longevity for the given thermodynamic profile and simulation design (Weisman et al. 1988). There is no initial north–south wind component because the component of shear perpendicular to the line is much more important to squall-line maintenance than is the line-parallel shear (Weisman et al. 1988).

Convection is initiated with a temperature anomaly 4 K warmer than its surroundings, on which random perturbations of 0.1 K are superposed. The thermal has a radius of 10 km in the east–west direction, a vertical radius of 1400 m, and is infinitely long in the north–south direction. It is centered at $x = 25$ km and $z = 1400$ m AGL.

Radiation, surface physics, and the Coriolis force are neglected in the simulations. Also, a warm-rain microphysical parameterization (Kessler 1969) is used for both computational efficiency and because ice processes have little effect on the convective zone of squall lines (e.g., Fovell and Ogura 1988; Yang and Houze

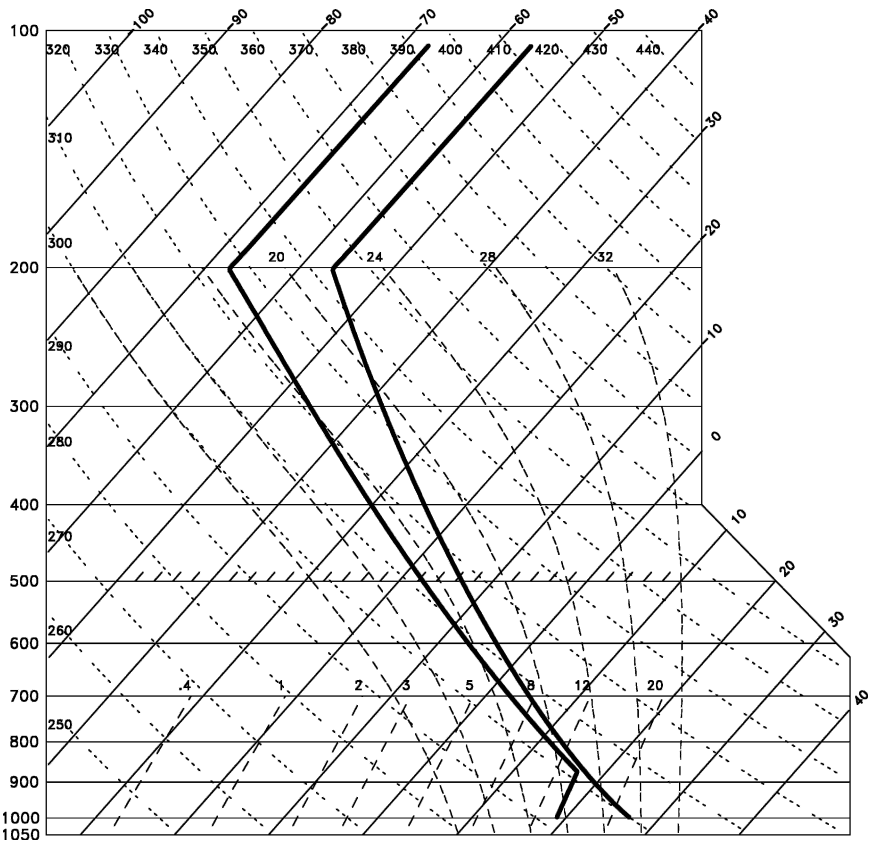

FIG. 1. Skew T–log$p$ diagram depicting the initial vertical temperature and moisture profile. Adapted from Weisman and Klemp (1982).

1995). ARPS employs a splitting technique, allowing the acoustic terms to be treated separately on a smaller time step (Klemp and Wilhelmson 1978). The simulations use a large time step of 6 s and a small step of 1 s.

The choice of a numerical damping coefficient is somewhat arbitrary because the coefficient does not represent a specific physical process. The challenge here is to use a large enough coefficient to sufficiently damp the artificial $2\Delta x$ waves, but not to use a coefficient so large that it begins to damp out important small-scale processes. The horizontal computational mixing coefficient is 1.22×10^9 m^4 s^{-1}, and the average vertical computational mixing coefficient is 3.13×10^7 m^4 s^{-1}. Lower values of numerical diffusion result in the development of a significant amount of spurious convection within the domain, like that reported by Adlerman and Droegemeier (2002). Our values of numerical diffusion restrict the development of spurious convection to the western edge of the domain, or about 300 km behind the squall line, after 4 h of simulation time. If a much larger value is used, the damping becomes so strong that it begins to significantly alter the behavior of the squall line.

b. Experiments

A suite of simulations was performed to investigate how various mountain ridge configurations affect squall lines. All ridges are parallel to the squall line, infinite in the y direction, and centered at the midpoint of the domain, $x = 200$ km. The terrain height, h, is defined by the following function:

$$h(x) = \begin{cases} H_0 \cos^2\left[\dfrac{\pi(x - x_{\rm cm})}{2x_{\rm rm}}\right], & x_{\rm cm} - x_{\rm rm} \le x \le x_{\rm cm} + x_{\rm rm} \\ 0, & \text{elsewhere} \end{cases}. \quad (1)$$

Here, H_0 is the height of the mountain, $x_{\rm cm}$ is the center point of the mountain, and $x_{\rm rm}$ is the radius of the mountain. The mountain height varies from 300 to 1800 m, and the radius varies from 10 to 40 km. The simulation with $H_0 = 900$ m and $x_{\rm rm} = 10$ km has been chosen for the archetypal ridge simulation because it produces a significant effect on the squall line. A schematic of the model grid for this setup is provided in Fig.

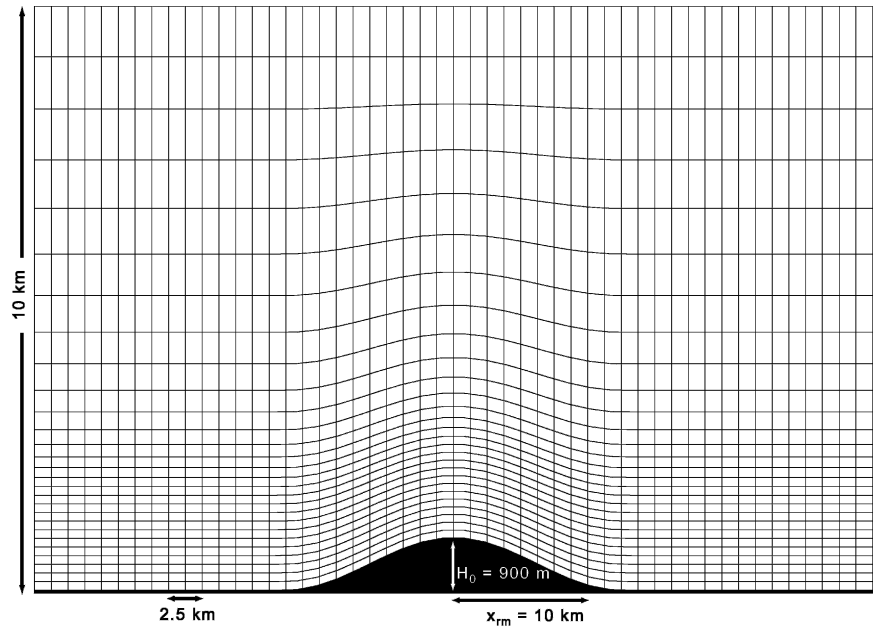

FIG. 2. Model domain and terrain configuration for the $H_0 = 900$ m, $x_{rm} = 10$ km ridge case. The vertical scale has been exaggerated and only a portion of the domain is shown. Grid lines are at every x grid point and every model vertical level below 10 km. The terrain is shown by the dark shading.

2. Although the slope of this mountain may seem extreme, it is actually less than that found on individual ridges within the Appalachian Mountains in parts of North Carolina, Virginia, and New York. Control simulations without an initial temperature perturbation are used to investigate how the mountains influence their environment. Additionally, a control simulation of a squall line traversing flat terrain with an elevation of 0 m is also presented.

3. Control simulations

a. Simulations with terrain and without convection

We conducted a set of simulations with no initial temperature perturbation in order to isolate the effects of the topography on its environment. The height of the mountain varies from 300 to 900 m, and x_{rm} ranges from 10 to 50 km. Deep moist convection fails to develop in all such simulations without an initial temperature perturbation. This is likely because of the homogeneity of the mountain ridge in the y direction, since a completely homogeneous thermal (i.e., with no random perturbations superposed) also fails to form a line of deep moist convection. In the case of a 900-m-high and 20-km-wide ($x_{rm} = 10$ km) ridge, the topography generates gravity waves (Fig. 3a). At low levels, a zone of subsidence is located from the mountain crest to about 5 km downstream of the crest (between $x = 200$ and 205 km), which is near the steepest slope of the terrain. The westerly winds in this same area are accelerated by 3–4 m s^{-1} above their base-state values. Farther downstream, near $x = 210$ km, there is a region of ascent, with a zone of vertical velocities extending through a greater depth as one gets farther downstream from the topography. Beyond $x = 220$ km, the magnitude of the low-level wind perturbations decreases substantially, as most of the wave energy propagates upward into the sponge layer. However, there is also a downstream component to the energy propagation. The horizontal and vertical wavelengths of these disturbances are both on the order of 10 km, and the maximum upward and downward vertical velocities are about 2 m s^{-1}. The structure of these perturbations suggests a gravity wave with phase lines that tilt upstream with height. As a result, the zonal wind maxima are well correlated with the vertical velocity minima and vice versa. All of these features are consistent with nonhydrostatic orographic gravity waves (e.g., Smith 1979; Dudhia 1993; Xue et al. 2000).

As the slope of the terrain decreases, the amplitude of the vertical velocity perturbations also decreases. For example, in the case of the ridge with $x_{rm} = 40$ km (Fig. 3b), the maximum steady-state vertical velocities are reduced by approximately a factor of 4 (Table 1),

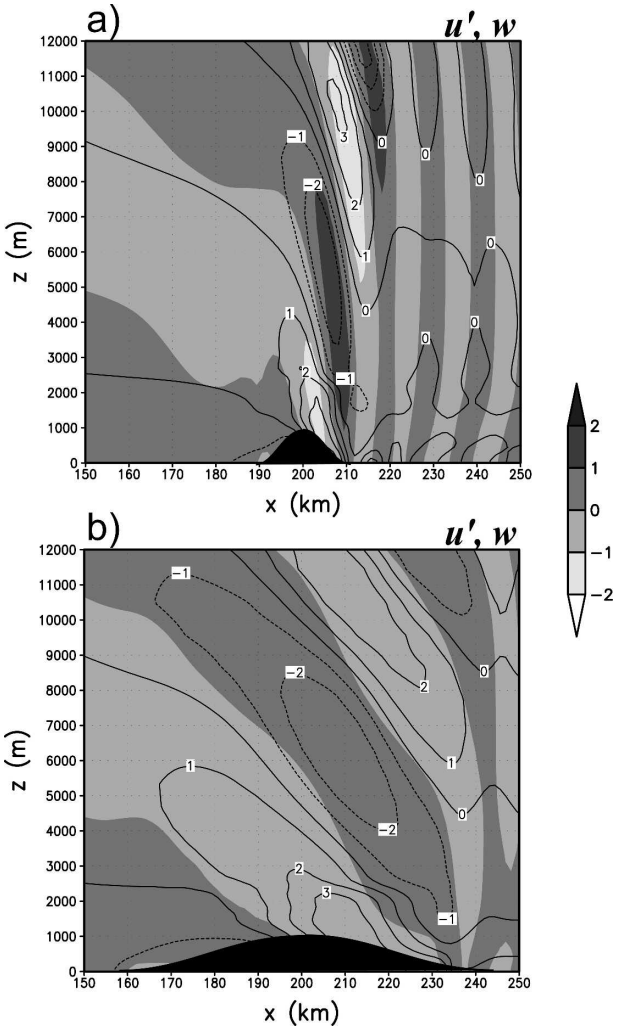

FIG. 3. Vertical cross sections showing the perturbation horizontal velocity u' (contoured; m s^{-1}) and the vertical velocity w (shaded; m s^{-1}) induced by orographic gravity waves for ridges with (a) $H_0 = 900$ m, $x_{rm} = 10$ km and (b) $H_0 = 900$ m, $x_{rm} = 40$ km. The u' contour interval is 1 m s^{-1} and the w shading interval is as indicated.

which is consistent with a fourfold decrease in slope magnitude. For a mountain with $H_0 = 300$ m and $x_{rm} = 10$ km, the magnitude of all perturbations decreases. The perturbations to the zonal wind, however, do not decrease nearly as much with decreasing slope (Table 1). The zonal wind perturbations also decrease with increasing mountain width, but not as much as do the vertical velocity perturbations. This indicates that the ray along which the gravity waves propagate makes an angle with the horizontal that decreases with mountain slope, which is an intuitive result. Also, the horizontal wavelength of the disturbances increases with the length scale of the topography.

All disturbances are independent of y and eventually reach a steady state. The time required to do so increases with the width of the mountain, ranging from under 1 h for $x_{rm} = 10$ km to just over 2 h for $x_{rm} = 50$ km. The longer time scale in the case of the more gradual slopes is due to the longer length scale involved in those cases.

TABLE 1. Maximum and minimum steady-state perturbations associated with orographic gravity waves.

H_0 (m)	x_{rm} (km)	u'_{min} (m s^{-1})	u'_{max} (m s^{-1})	w_{min} (m s^{-1})	w_{max} (m s^{-1})
900	10	−3.28	4.25	−1.77	1.73
900	20	−3.40	4.07	−1.19	0.99
900	30	−3.24	3.92	−0.75	0.63
900	40	−3.02	3.76	−0.52	0.45
600	10	−1.54	2.33	−0.82	0.87
300	10	−0.43	0.87	−0.22	0.25

The Froude number can be used to further investigate the behavior of flows near topography and may be defined as

$$\mathrm{Fr} = \frac{u}{NH_0}, \tag{2}$$

where u is the zonal wind speed, H_0 is the maximum height of the topography, and N is the Brunt–Väisälä frequency, given by

$$N = \sqrt{\frac{g}{\theta_v}\frac{d\theta_v}{dz}}, \tag{3}$$

where θ_v is the virtual potential temperature and g is the gravitational acceleration. In simulations with a squall line, portions of the cold pool reach saturation, especially over the upwind slopes of the mountain. In these cases, calculation of the Froude number for saturated air is necessary. The moist Froude number, Fr_m, is given by

$$\mathrm{Fr}_m = \frac{u}{N_m H_0} \tag{4}$$

in which the moist Brunt–Väisälä frequency has been substituted for the dry Brunt–Väisälä frequency calculated from the virtual potential temperature. The moist Brunt–Väisälä frequency is given by Durran and Klemp (1982)

$$N_m = \sqrt{\frac{g}{T}\left(\frac{dT}{dz} + \Gamma_m\right)\left(1 + \frac{Lq_s}{RT}\right) - \frac{g}{1+q_w}\frac{dq_w}{dz}}, \tag{5}$$

where the pseudoadiabatic lapse rate, Γ_m, is

$$\Gamma_m = \Gamma_d \frac{(1 + q_w)\left(1 + \dfrac{Lq_s}{RT}\right)}{1 + \dfrac{c_{pv}q_s + c_w q_l}{c_p} + \dfrac{\epsilon L^2 q_s}{c_p RT^2}\left(1 + \dfrac{q_s}{\epsilon}\right)}. \quad (6)$$

In these expressions, T is the temperature of the air, L is the latent heat of vaporization of water, q_s is the saturation mixing ratio of water vapor, R is the gas constant for dry air, q_w is the total mixing ratio of water substance, Γ_d is the dry-adiabatic lapse rate, c_{pv} is the specific heat capacity of water vapor, c_w is the specific heat capacity of liquid water, q_l is the liquid water mixing ratio, c_p is the specific heat capacity of dry air, and $\epsilon = R/R_v$ is the ratio of gas constants for dry air and water vapor.

For relatively small values of Fr, the upstream flow at low levels is blocked because the flow does not possess enough kinetic energy to overcome the potential energy of the topographic barrier. Parcels at some higher level, but still lower than the mountain height, may be able to ascend the terrain, however, because a smaller vertical excursion is required to do so. One can think of this in terms of a "dividing streamline," below which the flow cannot ascend the topography, but can do so above the dividing streamline. For Fr on the order of unity, however, most of the mean flow is able to pass over the topography because the height of the dividing streamline decreases with increasing mean Fr (Arya 1988, p. 257).

In the case of a low ridge ($H_0 = 300$ m; Fig. 4a), the Froude number ranges from near zero at the lowest levels to approximately one at the top of the ridge. If the mountain height is doubled to 600 m (Fig. 4b), the Froude number is halved, with blocking likely in the lowest few hundred meters. If the mountain height is further increased to 900 m (Fig. 4c), more of the flow in the low levels is blocked and cannot ascend the topography. If much of the low-level ambient flow was not blocked in this case, stronger upward motion on the windward side of the mountain than what is shown in Fig. 3a would be required by continuity constraints given a horizontal flow of less than 10 m s^{-1}. Changing the mountain width, however (Fig. 4d), has little effect on Fr.

b. Simulation with convection over flat terrain

In the simulation without terrain, the initial thermal generates a line of updrafts by 900 s of simulation time, which only persists for approximately 1800 s. The evaporation of rain from the initial convection creates a cold pool, which results in the initiation of new cells by 3600 s. These cells merge into a continuous line during the ensuing 2700 s, resulting in a squall line.

Plots of total accumulated rainfall can be a useful measure of squall-line intensity. Although the rainfall field lags the vertical motion field somewhat, it provides a cumulative perspective on the domain-wide intensity of the system over the entire model integration. A plot of total accumulated rainfall at 18 000 s (Fig. 5) reveals significant along-line structure to the squall line, which is common in three-dimensional simulations of squall lines (e.g., Coniglio and Stensrud 2001).

A line-averaged vertical cross section at 9300 s (Fig. 6a) depicts an area of convective updrafts, with an average intensity greater than 6 m s^{-1}, situated between $x = 185$ and 195 km. These updrafts propagate eastward at a nearly constant speed of 21 m s^{-1} between 9300 and 10 800 s. The multiple updraft maxima often present in these cross sections are illustrative of a line composed of two to three active cells at any time. Typically, new cells develop from an upward extension of the GFU, as observed by Smull and Houze (1985) and seen in the simulations of Fovell and Tan (1998) and Lin and Joyce (2001). These cells subsequently intensify and deepen, while moving rearward in a system-relative sense. Eventually, the cells begin to weaken because they are deprived of potentially warm and moist inflow by the newer cells in front of them. For example, at 9600 s (Fig. 6b), a new cell is developing from the GFU at $x = 200$ km, a mature cell is near $x = 190$ km, and a decaying cell is located at $x = 183$ km. There is a slight weakening trend in line-averaged updraft intensity between 9300 and 10 800 s, but an examination of individual cross sections (not shown) and of the cumulative rainfall distribution (Fig. 5) reveals that there are intense cells at 10 800 s, but that they are fewer in number than at 9300 s.

The gust front and convective updrafts move at approximately the same speed through 9900 s (Figs. 6a–c), but then the gust front begins to move faster than the convective updrafts after this time (Figs. 6d–f). This has also occurred in previous squall-line simulations (e.g., Rotunno et al. 1988) because the amount of cold air beneath the convective system increases with time, owing to the continuous evaporation of precipitation into the RTF flow. This can offset the balance between the cold pool circulation and the low-level shear, resulting in a weaker system (Rotunno et al. 1988). The next section shows that terrain features can significantly alter this squall-line structure and evolution.

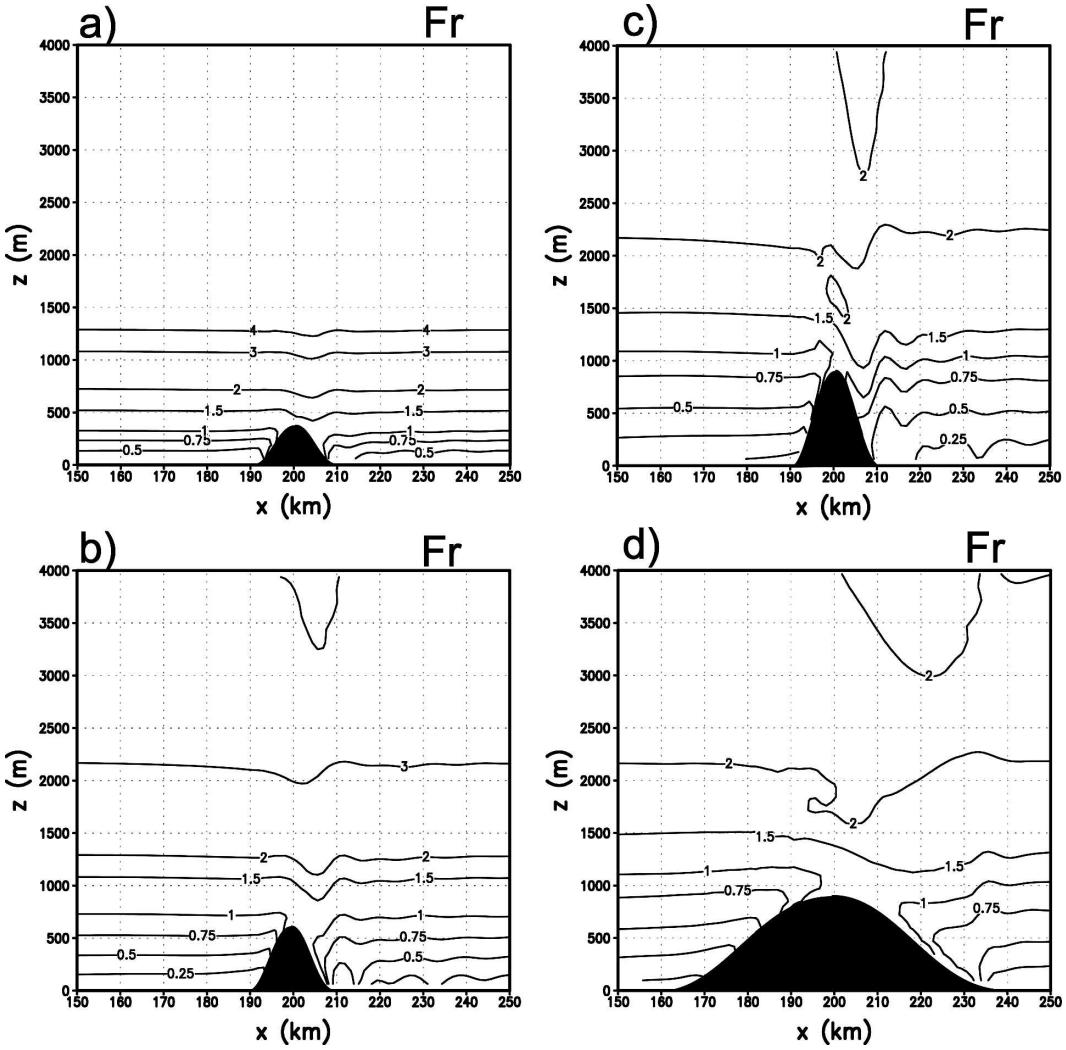

FIG. 4. Vertical cross sections showing the Froude number calculated relative to the height of the topography at 10 800 s for ridges with x_{rm} = 10 km and H_0 = (a) 300, (b) 600, (c) 900 m, and (d) x_{rm} = 40 km and H_0 = 900 m. Irregular contours are 0, 0.25, 0.5, 0.75, 1.0, 1.5, 2.0, 3.0, and 4.0.

4. Mountain ridge simulations

a. Mountain ridge archetype: H_0 = 900 m, x_{rm} = 10 km

The plot of total accumulated rainfall for the H_0 = 900 m, x_{rm} = 10 km ridge simulation (Fig. 7) is markedly different from that for the flat-terrain control simulation (Fig. 5). These differences are most pronounced over and just downstream from the mountain ridge. A zone of enhanced precipitation exists over the ridge, extending meridionally across the domain. This is followed by a stripe of significantly reduced rainfall downstream from the ridge, near x = 220 km. Finally, the total rainfall amounts increase again near x = 240 km. Within these minima and maxima, there is less along-line variability within the squall line compared with times before and significantly after the squall line traverses the ridge.

At 9300 s, the line-averaged cross section from the mountain simulation (Fig. 8a) looks similar to that from the control simulation (Fig. 6a). By 9600 s into the ridge simulation, the GFU weakens, becoming completely void of mean ascent greater than 6 m s^{-1} by 9900 s (Figs. 8b and 8c). The absence of strong ascent near the gust front is directly linked to a reduction in new cell formation there. The GFU resumes its original intensity by 10 200 s (Fig. 8d) and subsequently deepens, intensifies further, and maintains an erect structure through 10 800 s (Figs. 8e and 8f). The maximum mean updraft intensity at 10 800 s exceeds 9 m s^{-1}, which is the strongest seen over the period 9300–10 800 s between either the control or mountain ridge simulations.

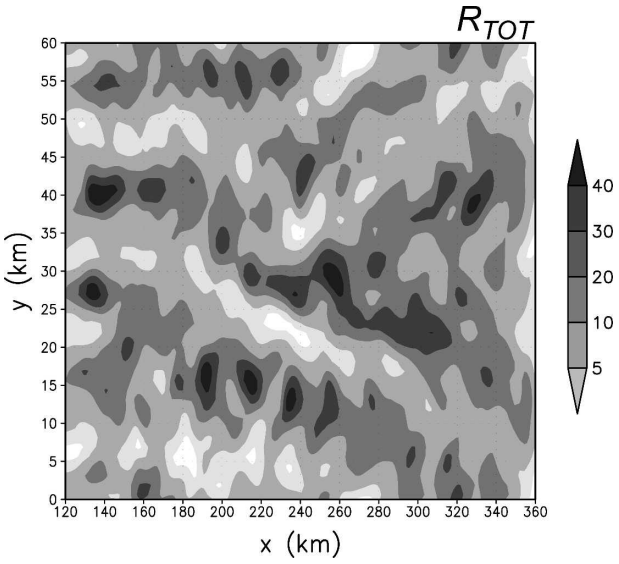

FIG. 5. Total accumulated rainfall (mm) at 18 000 s for the flat-terrain control simulation.

Also by 10 800 s, any older cells have weakened beyond recognition, and there is a zone of mean descent just behind the line of convection over the gust front.

As the gust front ascends and descends the mountain, its speed remains relatively constant. Its forward speed slows just following descent, as the position of the −2 K isotherm in the mountain ridge simulation is 2–3 km west of its position in the control run (cf. Figs. 6d–f and 8d–f). At the same time, the cold pool nose in the ridge simulation becomes steep and deep, and a dramatic reduction in depth is seen just behind the nose. This structure is indicative of a hydraulic jump; an in-depth discussion of its formation is found below.

There is a stark contrast between the squall line as it crosses the ridge and the one in the control simulation at the same time. The squall line in the control simulation exhibits a gradual weakening from 9300 to 10 800 s, while the squall line in the ridge simulation undergoes a rapid weakening followed by a rapid reintensification. Furthermore, the plots of total rainfall are nearly identical west of $x = 180$ km, but are not east of this point (Figs. 5 and 7). These variations in intensity, rainfall patterns, and gust front speed are a direct consequence of the interaction of the squall line with the terrain. Well east of the ridge, the squall lines in the two simulations have the same character, but the rainfall maxima and minima do not closely correspond with each other because of the prior disruption of the convective system in the ridge simulation.

A comparison of cross sections taken while the GFU is near $x = 195$ km (Figs. 6a and 8a) reveals that the cells in the simulation with the mountain ridge are stronger than those in the simulation with flat terrain. This result is also consistent with the plots of total rainfall, with a meridional rainfall maximum existing over the ridge in Fig. 7, but with no such pattern in Fig. 5. A system-relative streamline analysis (Fig. 9) indicates that most of the orographically forced ascent takes place behind the surface position of the gust front. At 9600 s, for example, there is greater ascent from $x = 190$ to 200 km in the mountain ridge simulation than in the flat-terrain simulation (cf. Figs. 9a and 9b). The cold pool is forced upward (notice the vertical motion at the top of the cold pool in Fig. 9b), which adds extra lift to the positively buoyant air above the cold pool. Thus, the orographic ascent within the cold pool adds extra forcing to the updrafts from below.

Aside from the new cell forming over the hydraulic jump, there is no mature cell seen in either mountain ridge simulation from 10 200 to 10 500 s. The reason for this is that no cells are initiated at the gust front between 9900 and 10 200 s (Figs. 8d and 8e), which is coincident with the descent of the gust front down the mountainside. A system-relative streamline analysis offers more detail of the flow structure as the squall line descends the slope (Fig. 10). During descent, the cold pool head also becomes shallower (Figs. 8c and 10b).

As the gust front descends the mountain, it first passes through a region of subsidence due to orographic gravity waves between $x = 200$ and 205 km, which likely contributes to the disappearance of the GFU during descent. The gust front then enters a region of upward vertical velocities near $x = 210$ km (Fig. 3a). Deep convective updrafts do not form at the front of the system until it has exited this favored region, however. Thus, the orographic gravity waves help to suppress the convection during descent, but are not responsible for the discrete propagation of the squall line downstream from the ridge.

To investigate the effects of density current dynamics and the hydraulic jump in the evolution of the squall line downstream from the ridge, plots of the Froude number within the cold pool are examined. The Froude number, as calculated previously, however, is a better indicator of orographic blocking than whether or not a flow is supercritical or subcritical because the denominator contains the mountain height as opposed to the depth of a fluid layer. If one considers the depth of the cold pool instead of the mountain height as H in (2), then it is possible to identify a flow as supercritical or subcritical (Fig. 11). While the cold pool is still deep, the Froude number near the gust front is less than one (Fig. 11a). As the cold pool descends the mountain, it becomes much shallower, and the Froude number in the cold pool head increases to greater than one (Fig.

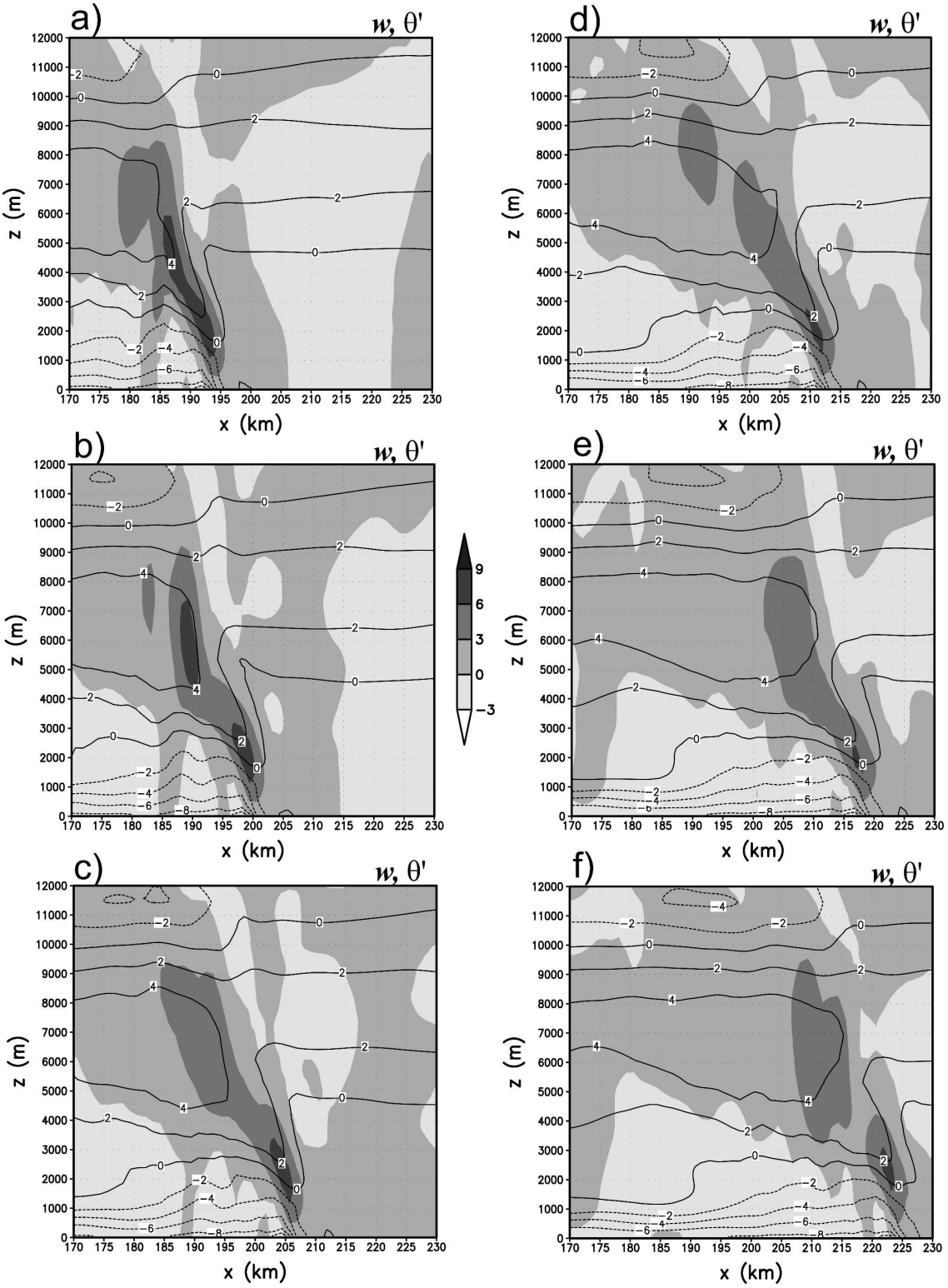

FIG. 6. Along-line-averaged vertical cross sections of w (m s^{-1}; shaded) and potential temperature perturbation θ' (K; contoured) in the control simulation for (a) 9300, (b) 9600, (c) 9900, (d) 10 200, (e) 10 500, and (f) 10 800 s.

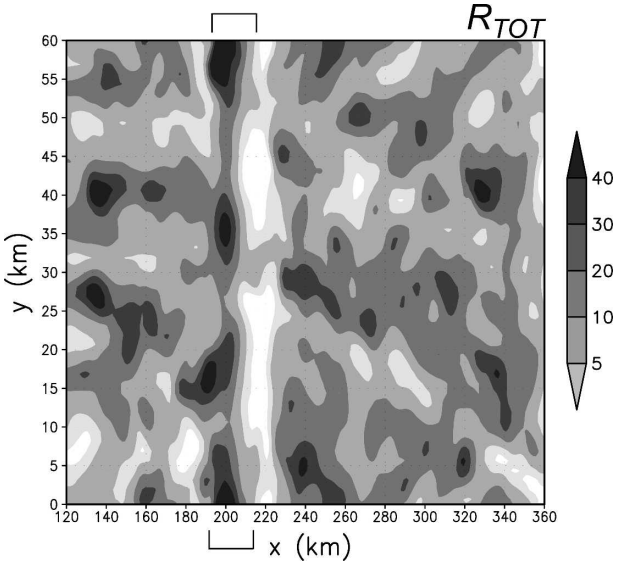

FIG. 7. As in Fig. 5 but for the H_0 = 900 m, x_{rm} = 10 km mountain ridge simulation. Brackets indicate the location of the mountain ridge.

11b). Also, the zonal flow accelerates slightly over the downslope because of the orographic gravity waves (Fig. 3a). Thus, the flow in the cold pool transitions from the deep subcritical flow seen in the entire control simulation (e.g., Fig. 10a) and in the mountain simulation up to the descent, to a shallow supercritical flow. A supercritical density current head creates much less lift than does a subcritical one owing to the absence of an overturning circulation in front of the density current (Xu et al. 1996), significantly reducing the likelihood of the initiation of new cells at the gust front during descent. When the gust front reaches the bottom of the hill, cold air begins to accumulate as the propagation speed of the gust front slows. Thus, the flow within the cold pool transitions back to subcritical following the descent. It is well known that as a flow transitions from a subcritical to a supercritical regime, a hydraulic jump forms (e.g., Kundu and Cohen 2002, 227–229). Hydraulic jumps are typically characterized by sharp differences in the depth of a fluid, similar to what is seen near x = 210 km in Figs. 8d–f and 10b. As a result of the hydraulic jump, the cold pool nose again becomes steep and deep, increasing the lift along the gust front. This lift results in the rapid initiation of new cells along the entire gust front, and in the increase in total precipitation downstream of the slope in Fig. 7. The convective minimum over the lee slope followed by the regeneration of the convection downstream results in discrete propagation of the squall line over the ridge in this case. Discrete propagation has also been observed in orographically induced convective systems in the lee of the Rocky Mountains (e.g., Grady and Verlinde 1997).

The primary cause of the shallow cold pool during its descent from the mountain is that some of the evaporatively cooled air present upwind of the topography is blocked by the mountain. A plot of the orographic Froude number just upwind of the mountain, near x = 190 km (Fig. 12b), suggests that it is possible that the cold pool is blocked over the lowest several hundred meters. A trajectory analysis (Fig. 13) provides more evidence for this blocking scenario. Trajectories a and b were initiated within the RTF jet (defined by the 10 m s^{-1} isotach) at 9000 s below the maximum height of the mountain, and traverse the topography without any blocking, as do all other trajectories like them. Trajectory f was initiated to the rear of, but at the same level as trajectories a and b, and was outside of the RTF jet. It, and all other trajectories like it, fail to ascend the mountain. Trajectories c–e were initiated in the same system-relative position as trajectory f (i.e., to the rear of the descending RTF jet) but at 900 s later than these other trajectories. Back trajectories to 9000 s were also computed for trajectories c–e. Trajectory c was in the RTF jet at 9000 s, but descends below it by 9900 s, and still traverses the mountain. Trajectory d, which is at the same level as trajectory c at 9900 s, is blocked and fails to cross the orography. Of the trajectories in this group, approximately half were able to cross the mountain. Trajectory e was initiated below the level of trajectories c and d at 9900 s, and it and all others in its group are blocked. Thus, air parcels within the RTF jet are able to ascend the mountain owing to their large kinetic energy, as are some of the parcels just below/behind the descending branch of this jet. Based on this analysis, we conclude that all saturated parcels with a moist Froude number less than 0.5 are blocked, all unsaturated parcels with a dry Froude number less than 0.25 are blocked, and some saturated parcels with a moist Froude number between 0.5 and 0.75 are also blocked (Figs. 12c and 12d), as are some unsaturated parcels with dry Froude numbers between 0.25 and 0.5. The air that is blocked includes the large mass of cold air beneath the RTF jet once the jet has ascended the ridge (Figs. 12a, 12c, and 12d). Further substantiation for this claim is offered by a horizontal wind analysis (Figs. 12c and 12d). At 9600 s (Fig. 12c), flow less than 5 m s^{-1} extends through a layer approximately 500 m deep, but this air is still 10–15 km west of the ridge, and has yet to experience any orographic blocking. By 10 500 s (Fig. 12d), the RTF jet has ascended the ridge and this mass of slow-moving low-level cold air is banked up against the western slope of the ridge. The flow decelerates through a greater depth over the slope, and a

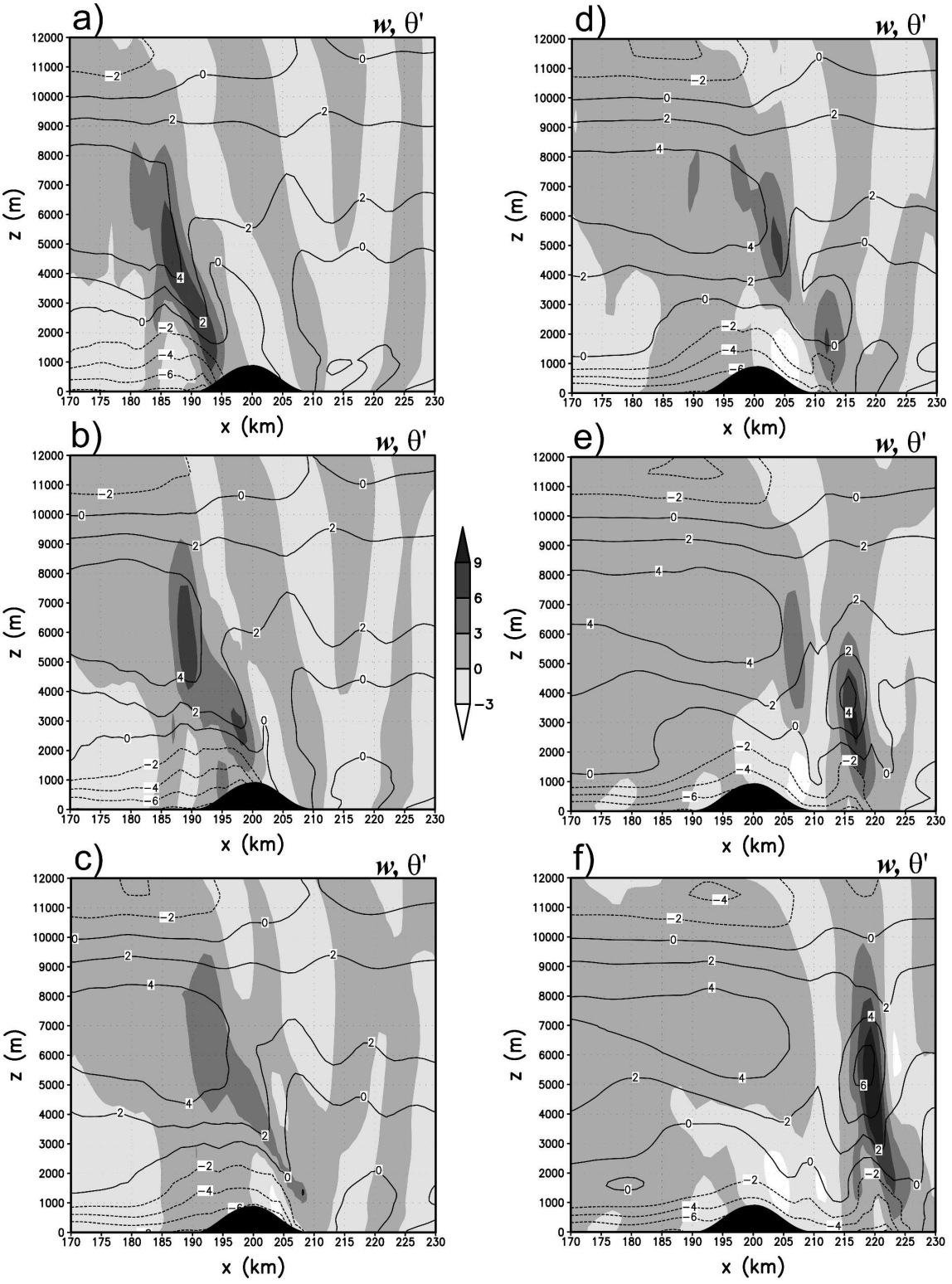

FIG. 8. As in Fig. 6 but for the H_0 = 900 m, x_{rm} = 10 km mountain ridge simulation for (a) 9300, (b) 9600, (c) 9900, (d) 10 200, (e) 10 500, and (f) 10 800 s.

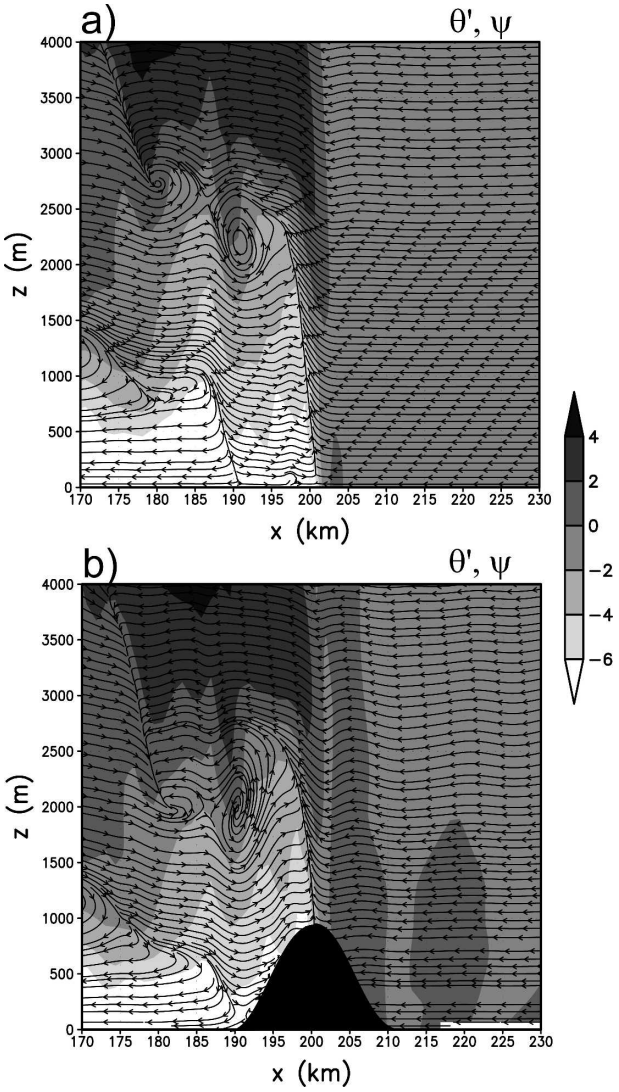

FIG. 9. System-relative streamline analysis and θ' (shaded) at 9600 s for (a) the flat-terrain control simulation and (b) the H_0 = 900 m, x_{rm} = 10 km mountain ridge simulation. A propagation speed of 20 m s^{-1} has been subtracted from the zonal wind component to create a system-relative velocity profile.

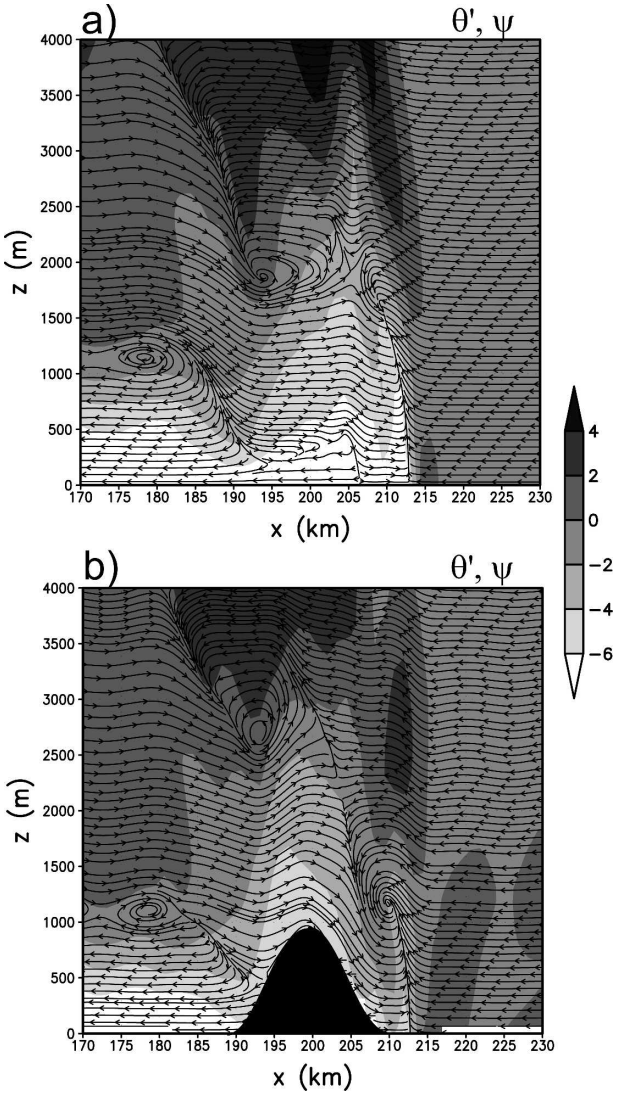

FIG. 10. As in Fig. 9 but at 10 200 s for (a) the control simulation and (b) the H_0 = 900 m, x_{rm} = 10 km ridge simulation.

layer of easterly flow 200–300 m deep develops in response to the orographic blocking.

The lack of cold air on the lee side of the mountain results in a shallower cold pool, less lift, and ultimately less precipitation, as discussed above. This reduction in precipitation is a secondary effect that limits the amount of fresh cold air entering the cold pool owing to evaporative processes. A third effect weakening the cold pool is the adiabatic warming of the cold air during descent. Given the lack of precipitation over the downslope, the cold air that descends the mountainside evaporates a relatively small amount of precipitation during descent, unlike the rainy downdraft air descending from a thunderstorm over level terrain. Taken together, these processes reduce temperature deficits within the cold pool from 6 to 8 K upstream of the mountain to approximately 2 K immediately downstream from it (Fig. 8). Both the depth of cold air and the temperature deficit within the cold pool are crucial to maintaining the lift at the gust front and a long-lived convective system (Rotunno et al. 1988).

Additionally, the terrain affects the horizontal wind field. Comparing the winds from the control simulation (Fig. 14a) to those from the mountain ridge simulation (Fig. 14b), there is a more widespread area of potentially damaging winds greater than 25 m s^{-1} in the ridge simulation. This is partially because of the larger area covered by significant convection following the passage

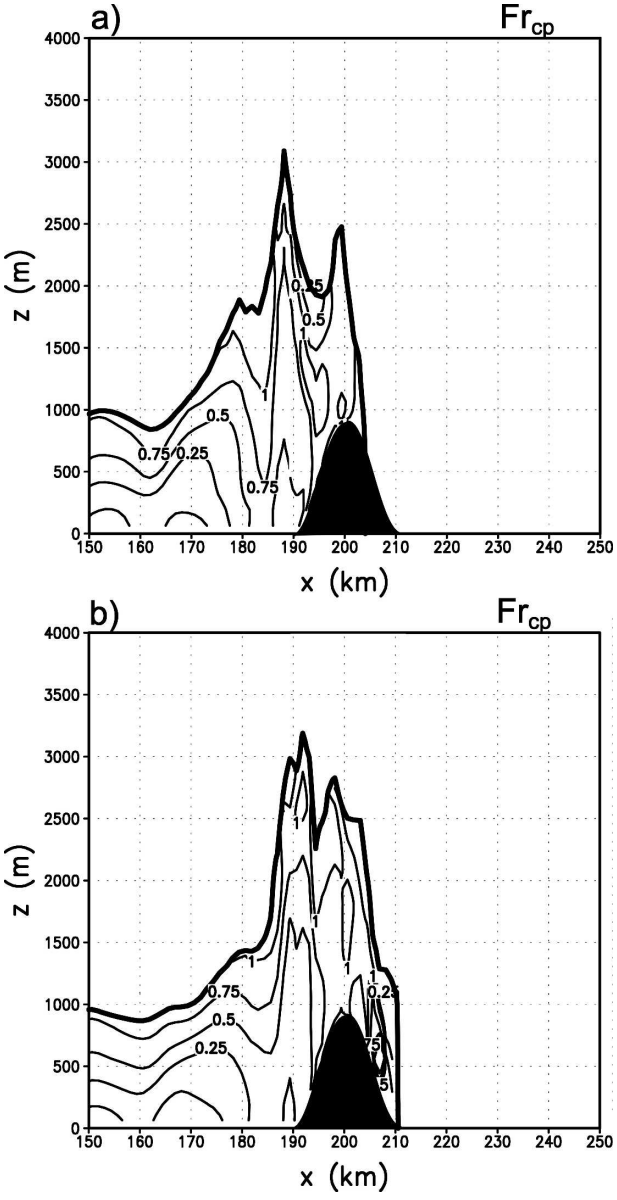

FIG. 11. Froude number calculated relative to the cold pool depth (Fr_{cp}) for the squall-line simulation over a ridge with H_0 = 900 m, x_{rm} = 10 km at (a) 9600 and (b) 9900 s. The boldface black line indicates the position of the −1 K isotherm. The contour interval is as in Fig. 4.

of the squall line over the topography. Further substantiation for this argument between convection and winds can be seen by comparing the horizontal wind maxima (Fig. 14a) to the precipitation maxima (Fig. 5) in the control simulation. The negative buoyancy of the cold pool during descent also contributes to this increase in wind speed.

Mahrer (1984) recommends that the increase in terrain height between two horizontal grid points should not exceed the vertical grid spacing in the model. This is not the case for all of the simulations because of the computational limitations discussed above. The archetypal ridge simulation has been reproduced at 500-m horizontal grid spacing, which meets the guidelines set forth in Mahrer (1984). The total rainfall plot from this simulation (Fig. 15) looks similar to that from the simulation with 1.25-km grid spacing, with the orographically forced precipitation maximum over the ridge, followed by a distinct precipitation minimum downstream. A vertical cross section taken just after descent (not shown) also shows the hydraulic jump downstream of the topography, proving that the above evolution is not a consequence of insufficient horizontal resolution.

Although investigations between preexisting convection and terrain have been limited, there have been several studies published regarding the interaction between cold fronts and terrain. In the case of an intense cold front descending the Appalachian Mountains, Koch and Kocin (1991) observed the formation of both a narrow cold frontal rainband and a hydraulic jump in the lee of the mountain range. The observations in this case, however, were inadequate to determine the exact role orography played in the initiation of these features. In numerical simulations of this same event, Chen et al. (1997) also found a rain shadow over the lee slopes of the mountains, with the formation of a line of precipitation downstream. They ultimately conclude that the mountains do not play a major role in this process, but Koch (1999) noted that this may be because of the use of smoothed terrain in their model. As a result of this, the slope of the terrain in their study is significantly less than in any of the simulations presented here. Additionally, dry simulations of a cold front (Williams et al. 1992) and of a density current (Bischoff-Gauss et al. 1989) moving over a mountain ridge both reveal hydraulic jump formation at the base of the lee slope, as in the simulations presented above.

In a numerical study of mountain-induced convection over a sinusoidal ridge, Chu and Lin (2000) also found a rain shadow over the downslope portion of the terrain. Convection developed over the upslope region and downstream of the ridge. Convective enhancement also occurs over the same areas in this study.

b. Variable mountain width simulations

In the case of a ridge with x_{rm} = 40 km, one would expect the squall line to be in a terrain-induced weaker state for a longer period of time because it takes longer for the convective system to move 80 km than it does for it to move 20 km. The plot of total accumulated rainfall (Fig. 16) supports this idea. There is a large area of orographic precipitation enhancement, extending

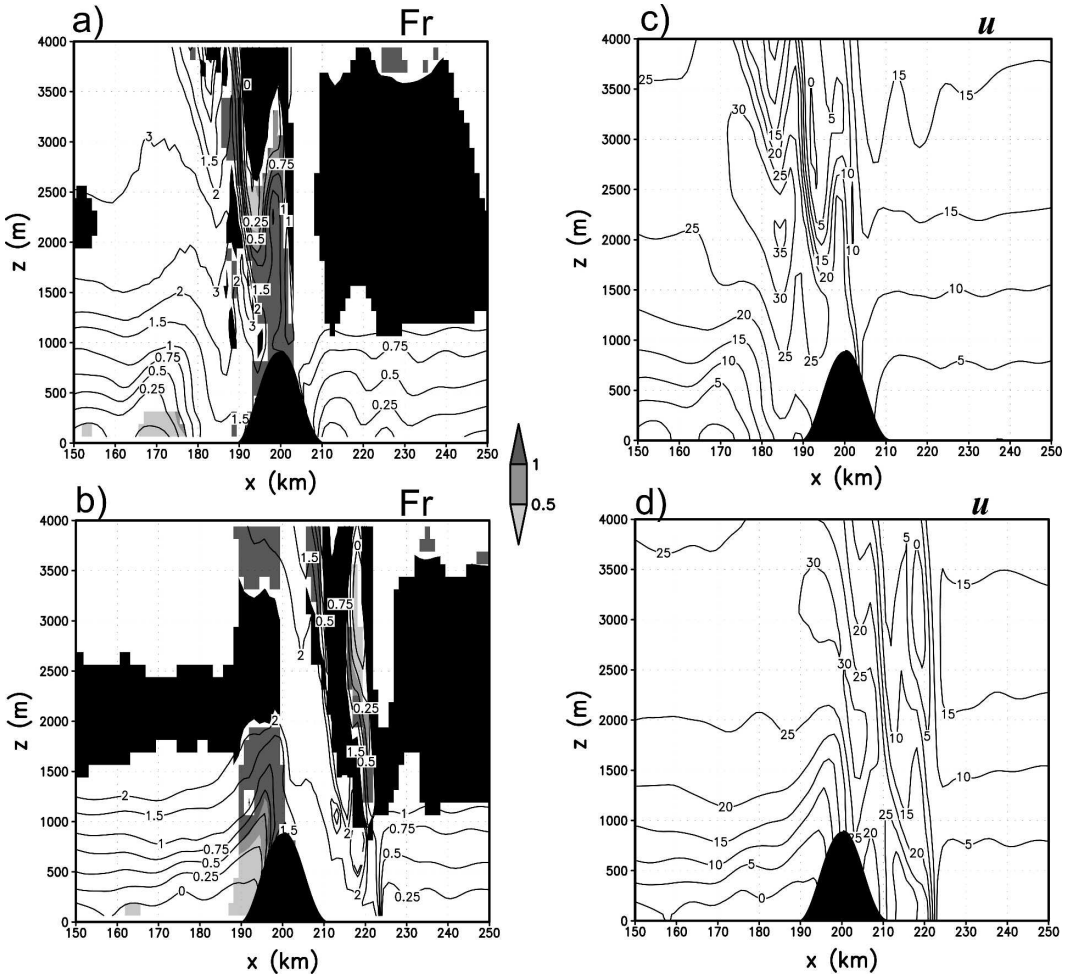

FIG. 12. As in Fig. 4 but for the squall-line simulation over a ridge with $H_0 = 900$ m and $x_{rm} = 10$ km at (a) 9600 and (b) 10 500 s. Vertical cross section of zonal wind speed (m s^{-1}) for the same simulation at (c) 9600 s and (d) 10 500 s. The contour interval in (c) and (d) is 5 m s^{-1}. The shading in (a) and (b) indicates the moist Froude number in regions where the relative humidity is greater than 95%. The blacked-out regions indicate regions where the moist Brunt–Väisälä frequency is undefined and the relative humidity is greater than 95%.

west of the base of the upslope, to around $x = 130$ km. This is consistent with the results presented above, in that most of the orographic ascent occurs behind the gust front and that the convective updrafts within a squall line slope rearward with height (e.g., Fig. 8). Thus, the zone of orographically enhanced precipitation appears to be of a larger scale than the slope itself.

There is still a pronounced minimum in precipitation

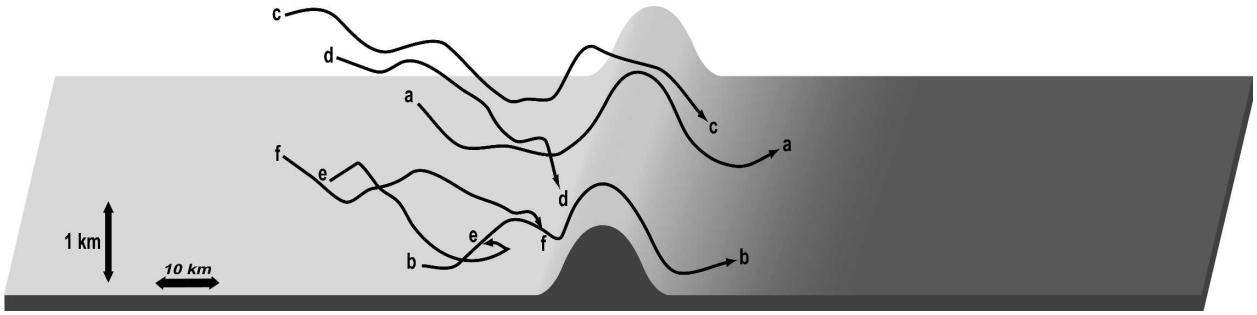

FIG. 13. Trajectory analysis of parcels in the $H_0 = 900$ m, $x_{rm} = 10$ km mountain ridge simulation. Vertical scale is stretched as indicated. See text for explanation of trajectories.

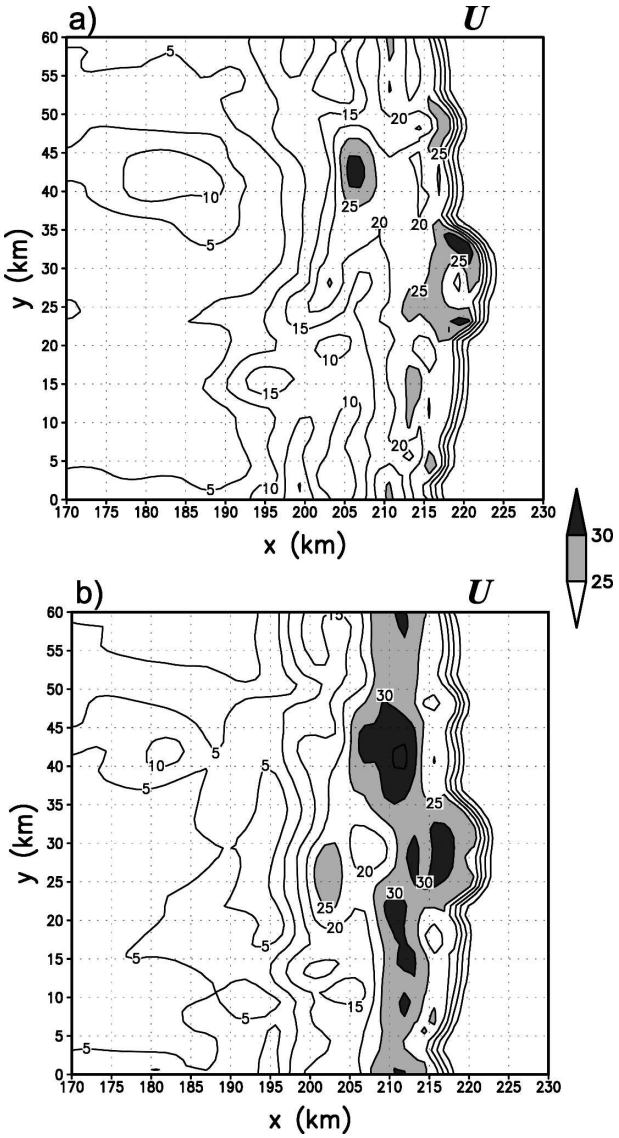

FIG. 14. Plan view of $z = 75$ m above ground level total horizontal wind speed at 10 500 s for (a) the control simulation and (b) the $H_0 = 900$ m, $x_{rm} = 10$ km ridge simulation.

because of the downslope, roughly between $x = 215$ and 240 km (Fig. 16). This region is narrower than the scale of the topography, in contrast to the result presented above. A line-averaged vertical cross section taken during descent at 10 200 s (Fig. 17a) indicates that the gust front head is still shallow when compared with a nondescending density current, inhibiting the initiation of convection for at least a portion of the descent. The Froude number in this case is substantially less than in the case with $x_{rm} = 10$ km (Fig. 18a) because the increased rainfall over the upwind slope results in colder outflow, greater static stability, and a lower Froude number. As a result, there is significantly more

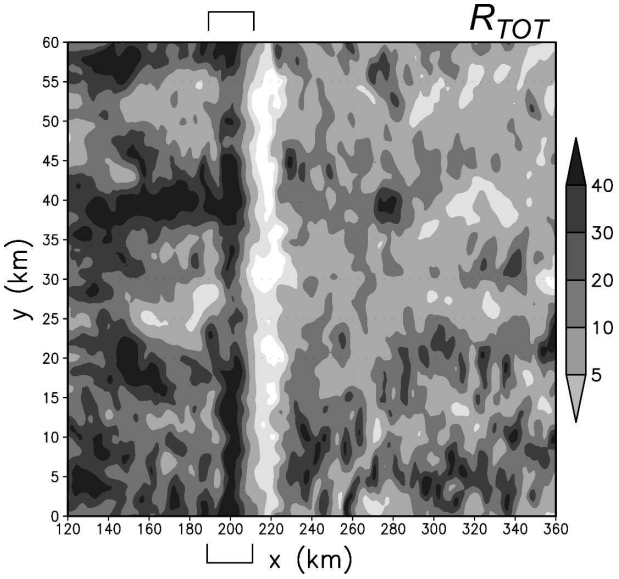

FIG. 15. As in Fig. 5 but for the $H_0 = 900$ m, $x_{rm} = 10$ km mountain ridge simulation with 500-m grid spacing. Brackets indicate the location of the mountain ridge.

blocking in this case than in the archetype, as depicted by a horizontal wind analysis (Fig. 18b), which shows a large area with $u < -5$ m s^{-1} near the surface between $x = 155$ and 170 km.

There is again a hydraulic jump in the outflow, which develops before the terrain completely levels off (Fig. 17b), owing to the gradual slope of the surface between

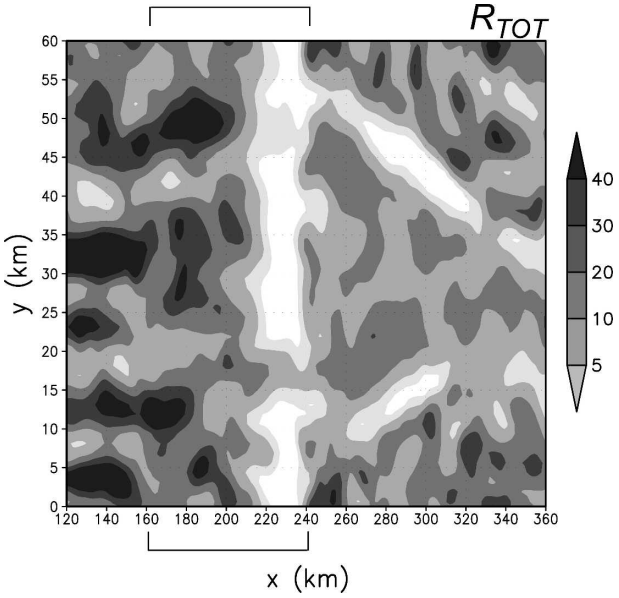

FIG. 16. As in Fig. 5 but for the $H_0 = 900$ m, $x_{rm} = 40$ km mountain ridge simulation. Brackets indicate the location of the mountain ridge.

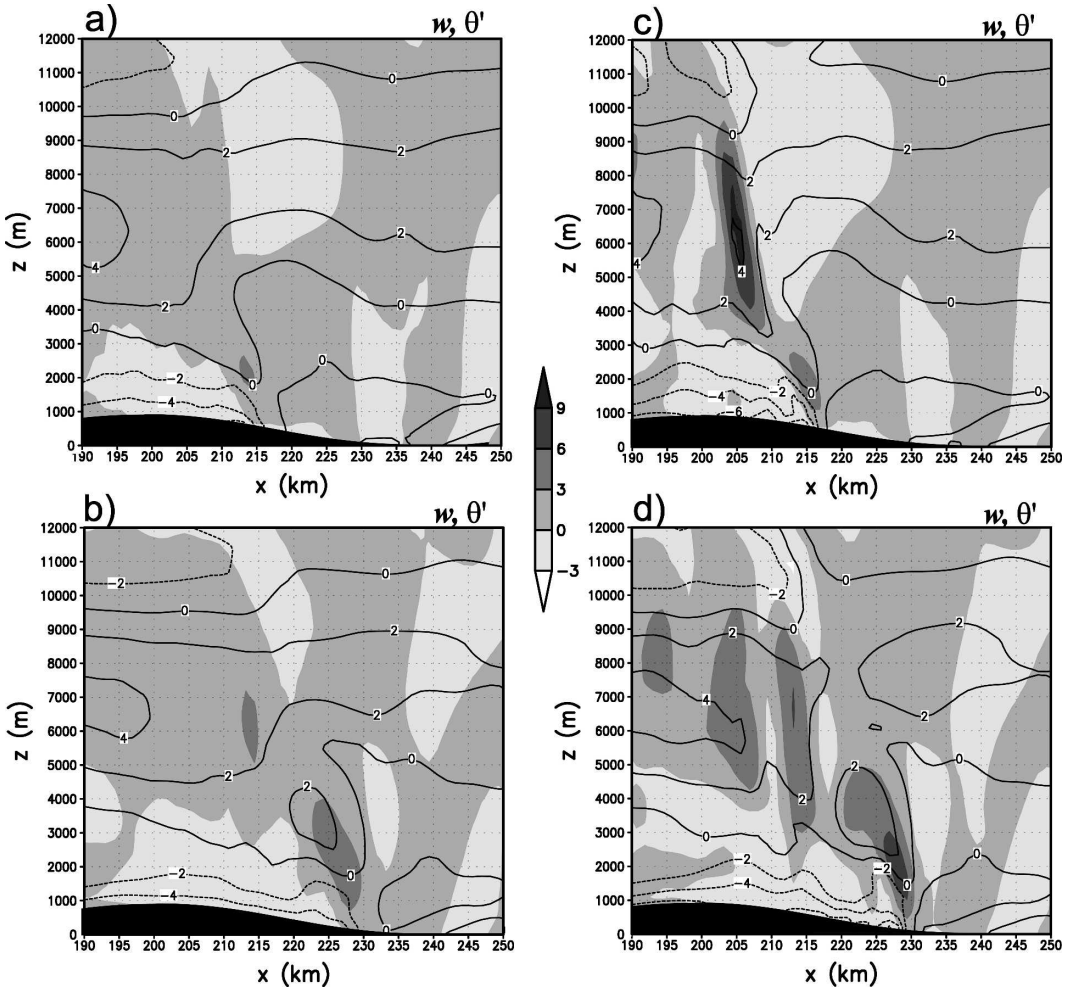

FIG. 17. As in Fig. 6 but for the H_0 = 900 m, x_{rm} = 40 km mountain ridge simulation at (a) 10 200 and (b) 10 800 s. Vertical cross sections taken at y = 35 km at (c) 10 200 and (d) 10 800 s.

x = 230 and 240 km. This hydraulic jump is clearer in nonaveraged vertical cross sections (Figs. 17c and 17d) than in line-averaged cross sections because it is not as prominent as in the archetypal simulation owing to the reduced slope. The longer downslope also prohibits the hydraulic jump from reinitiating convection for a longer period of time, resulting in a more prolonged precipitation minimum over the downslope than in the archetypal case above. Thus, the increase in total precipitation downstream of the mountain is more gradual in this case, because of less convergence from the reduced slope, a smaller hydraulic jump, and areas of subsidence aloft, like along y = 53 km (not shown).

c. *Variable mountain height simulations*

1) HIGH RIDGE: H_0 = 1800 M, x_{rm} = 10 KM

The plot of total accumulated rainfall for the simulation with an 1800-m-high, 20-km-wide ridge (i.e., twice the height but the same width as the archetype) indicates the same pattern as that presented above, only with a stronger signal because of more intense forcing from higher terrain and steeper slopes (Fig. 19). Intense rainfall occurs over the ridge, with some areas receiving over 100 mm of total precipitation. Although this ridge is an extreme example in its slope, these results highlight the risk of flooding from linear convective systems over steep topography. Nearly all of this precipitation is due to the passage of the squall line over the topography, and is not caused by secondary convection behind the squall line.

The terrain-induced minimum in rainfall is also still present in this case, with large areas just downstream from the ridge receiving less than 5 mm of total rainfall. The height of the −2 K isotherm (a proxy for cold pool depth) in this simulation is about 2000 m, which is virtually identical to the 900-m-high ridge simulations (e.g., Figs. 8a–f). Thus, almost the entire cold pool is

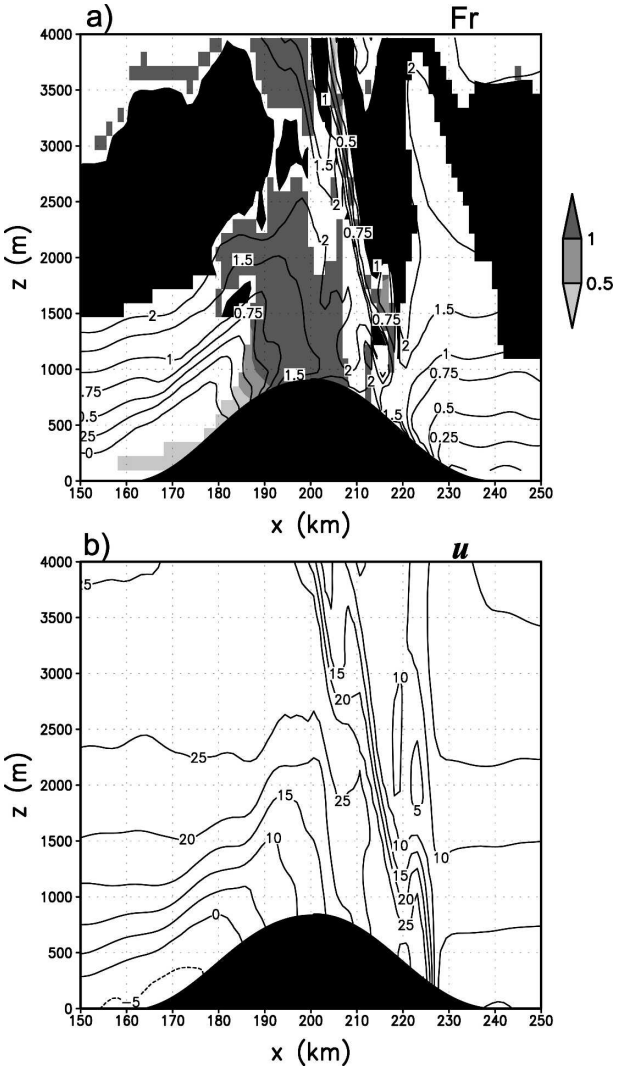

FIG. 18. (a) As in Fig. 4 but for the $H_0 = 900$ m, $x_{rm} = 40$ km mountain ridge simulation at 10 500 s. Shading is as in Fig. 12. (b) As in Fig. 12c but for the $H_0 = 900$ m, $x_{rm} = 40$ km mountain ridge simulation at 10 500 s.

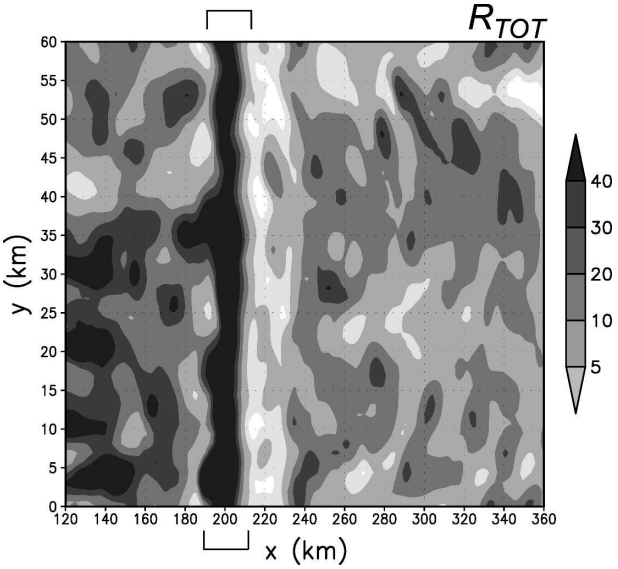

FIG. 19. As in Fig. 5 but for the $H_0 = 1800$ m, $x_{rm} = 10$ km mountain ridge simulation. Brackets indicate the location of the mountain ridge.

blocked. A horizontal wind analysis (Fig. 20b) also indicates that there is more blocking in the case of an 1800-m-high ridge than there is in the case of a 900-m high ridge (the 0 and 5 m s^{-1} isotachs are higher in Fig. 20b than in Fig. 12d). This increase in blocking is also consistent with the definition of the Froude number in (2), in which a twofold increase in mountain height results in a twofold decrease in the Froude number (not shown). This analysis also explains the more pronounced precipitation minimum in this case (Fig. 19). A hydraulic jump again is evident downstream from the mountain (Fig. 20a), resulting in regeneration of the convective line near the lee slope of the mountain, as in previous simulations.

The wind field at the bottom of the slope in the 1800-m case does not deviate significantly from what has already been presented in reference to the 900-m ridge. Furthermore, a higher mountain is at a greater risk for damaging winds because it is closer to the core of the RTF jet (Fig. 20b).

2) LOW-RIDGE SIMULATIONS

In the case of a 300-m-high ridge, the total rainfall plot reveals that the squall line is nearly unaffected by its passage over the 300-m-high topography (Fig. 21). In addition, a plan-view horizontal wind analysis (not shown) indicates that there are only isolated occurrences of near-surface winds greater than 30 m s^{-1} in the 300-m case, contrasting with the widespread occurrences of these potentially damaging winds in the 900-m simulations.

It is clear from a plot of the Froude number (Fig. 22) that the cold pool becomes less blocked as mountain height decreases because of increasing orographic Froude number values at any given altitude. In the 300-m case, for example, the Froude number does not become sufficiently low for blocking either saturated or unsaturated air until about 40 km behind the gust front, meaning that an ample amount of cold air is able to spill over the ridge and maintain the squall line (Fig. 22a). A line-averaged vertical cross section from the 300-m experiment (Fig. 23a) also shows a nearly 2000-m-deep layer of cold outflow moving across a 300-m-high ridge. This ridge is not high enough to block a sufficient

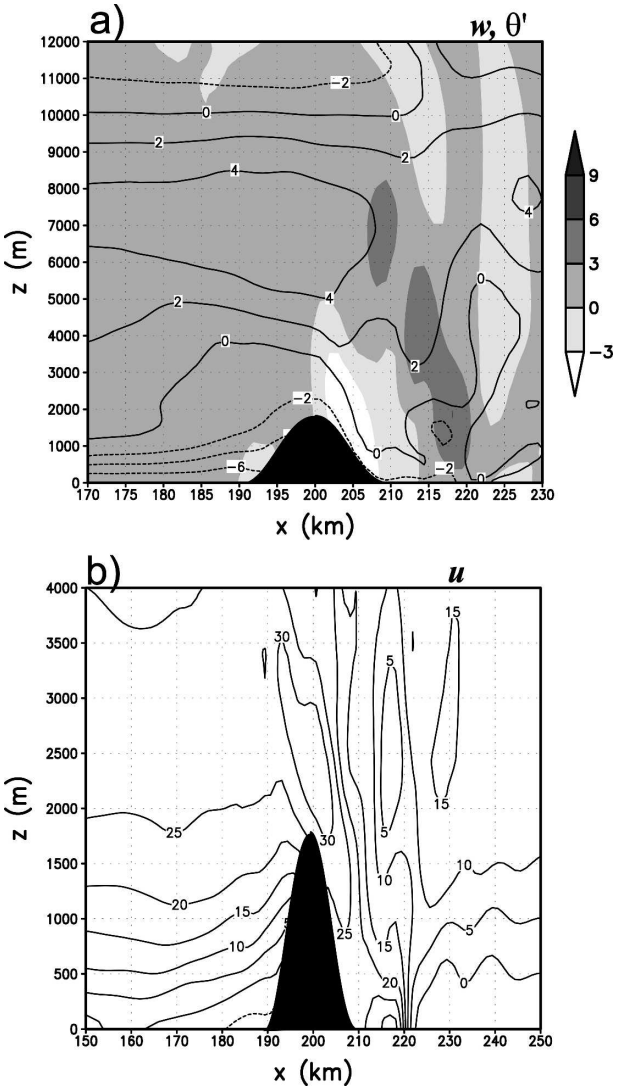

FIG. 20. (a) As in Fig. 6 but for the H_0 = 1800 m, x_{rm} = 10 km mountain ridge simulation at 10 500 s. (b) As in Fig. 12c but for the H_0 = 1800 m, x_{rm} = 10 km mountain ridge simulation at 10 500 s.

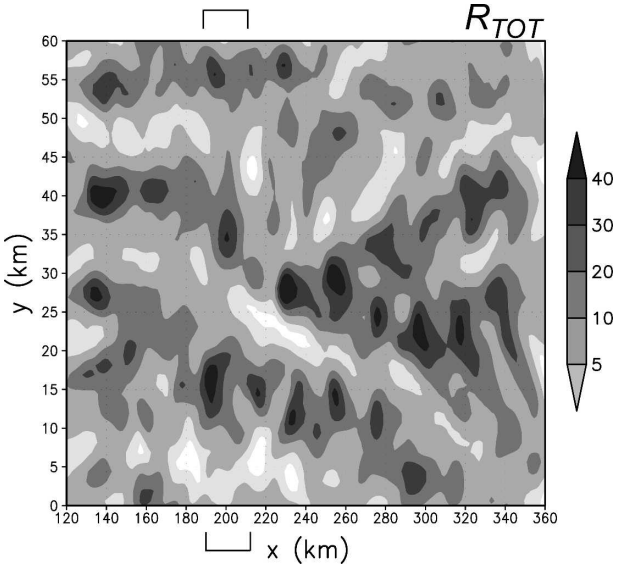

FIG. 21. As in Fig. 5 but for the H_0 = 300 m, x_{rm} = 10 km mountain ridge simulation. Brackets indicate the location of the mountain ridge.

amount of cold air to impact the squall line, as is clearly illustrated by this cross section. Furthermore, a horizontal wind plot at 10 500 s (Fig. 23b) indicates only a small amount of flow stagnation near x = 190 km in the lowest 100–200 m of the domain. At 500 m in elevation near the western slopes of the 300-m mountain, the zonal wind is about 3 m s^{-1} stronger than at the same place relative to the 900-m mountain, owing to less blocking. At z = 500 m, the air is already at a sufficient elevation to traverse the 300-m-high ridge, but would need to ascend another 400 m to traverse the 900-m-high ridge.

For a 600-m-high ridge (Figs. 22b and 24b), there is more blocking than in the 300-m case, but not as much as in the 900-m case because most saturated air is still able to flow over the mountain. Line-averaged vertical cross sections for this simulation (Fig. 24a) show less cold air on the lee side of the ridge than in the 300-m-high example, but more than in the 900-m-high archetype. The total rainfall plot (Fig. 25) bears this out, also showing a pattern similar to the 900-m case (Fig. 7), but smaller in magnitude. This squall line continuously propagates across this ridge, although it is in a weakened state over the lee slope.

To determine how high a mountain ridge must be to have an appreciable effect on a squall line, we performed a series of simulations in which the ridge height varied from 100 to 900 m at 100-m increments. There is no single mountain height where the topography begins to influence the squall line; rather, the topographical impact increases with the height of the terrain (cf. Figs. 7, 21, and 25). An analysis of the output reveals that discrete propagation occurs only when $H_0 > 600$ m. If the elevation of the topography is lower than this, the squall line continuously propagates across the terrain. Thus, for discrete propagation to occur, the mountain must be high enough both to block a significant portion of the cold outflow and to warm the outflow that is not blocked through adiabatic descent from the ridgetop. Clearly, these factors will also depend on environmental conditions such as the height of the RTF flow and the depth of the outflow beneath the convective line.

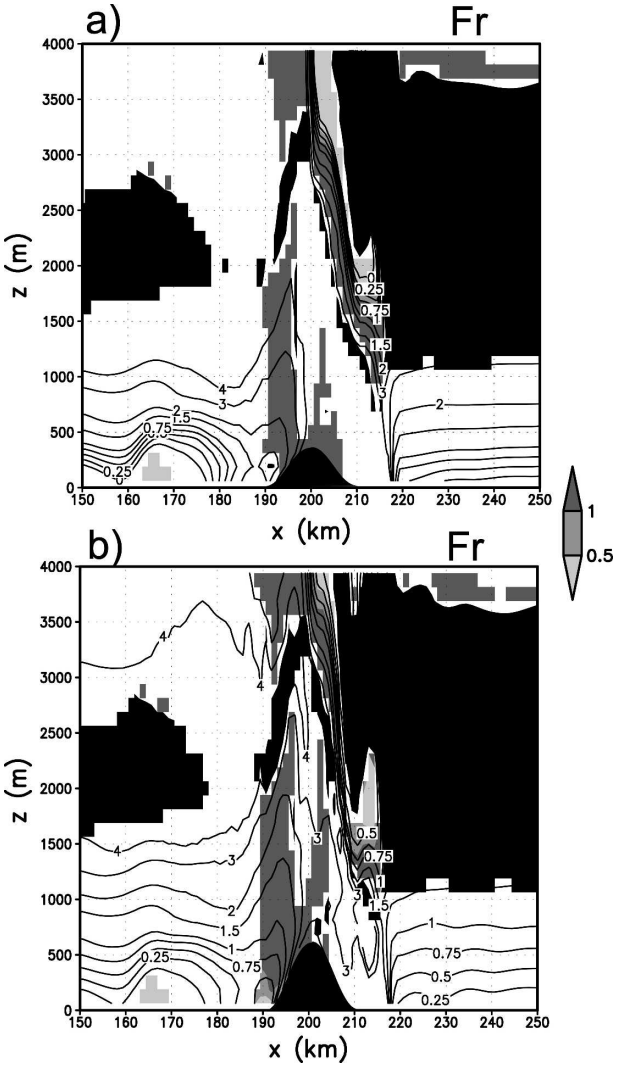

FIG. 22. As in Fig. 4 at 10 200 s but for the squall-line simulations over ridges with $x_{rm} = 10$ km and (a) $H_0 = 300$ m and (b) $H_0 = 600$ m. Shading is as in Fig. 12.

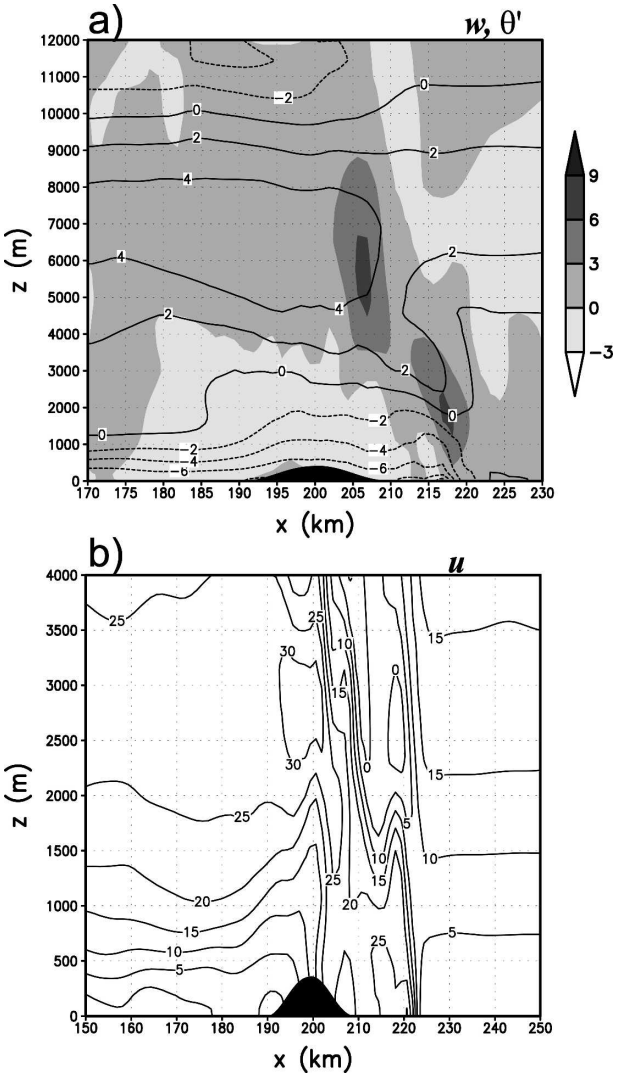

FIG. 23. (a) As in Fig. 6 but for the $H_0 = 300$ m, $x_{rm} = 10$ km mountain ridge simulation at 10 500 s. (b) As in Fig. 12c except for the $H_0 = 300$ m, $x_{rm} = 10$ km mountain ridge simulation at 10 500 s.

d. Multiple-ridge simulations

In the case of multiple ridges, the same rainfall pattern is produced each time the squall line encounters a ridge (Fig. 26). As the convective line traverses the first ridge, there is again orographic precipitation enhancement over the ridge and a rain shadow downwind of the ridge. The same signature is also visible in response to the second ridge, which is centered at $x = 240$ km.

Vertical cross sections (Fig. 27) also show similar behavior when a squall line encounters a second ridge. At 10 800 s, the line of updrafts that formed out of the hydraulic jump downstream of the first ridge is located over $x = 220$ km (Fig. 27a). These cells propagate eastward to $x = 225$ km and weaken by 11 400 s (Fig. 27b), while a new orographically enhanced cell develops near $x = 230$ km. The gust front is near the top of the second mountain at this time. By 12 000 s (Fig. 27c), the gust front has descended the second ridge and begins to form a hydraulic jump near $x = 250$ km. If the separation between the two ridges is increased to 40 km, or four times the radius of each ridge, the behavior is nearly identical (not shown). Thus, a second ridge influences a squall line in a manner very similar to a single ridge.

5. Summary and conclusions

The simulations presented herein reveal that squall lines undergo a process of orographic enhancement,

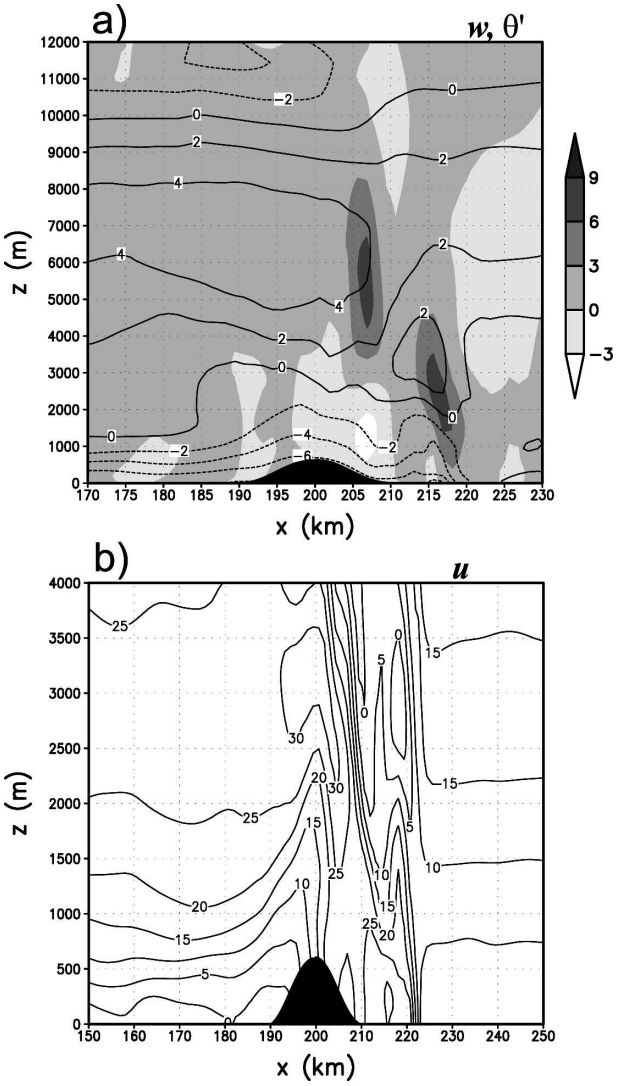

FIG. 24. (a) As in Fig. 6 but for the H_0 = 600 m, x_{rm} = 10 km mountain ridge simulation at 10 500 s. (b) As in Fig. 12c except for the H_0 = 600 m, x_{rm} = 10 km mountain ridge simulation at 10 500 s.

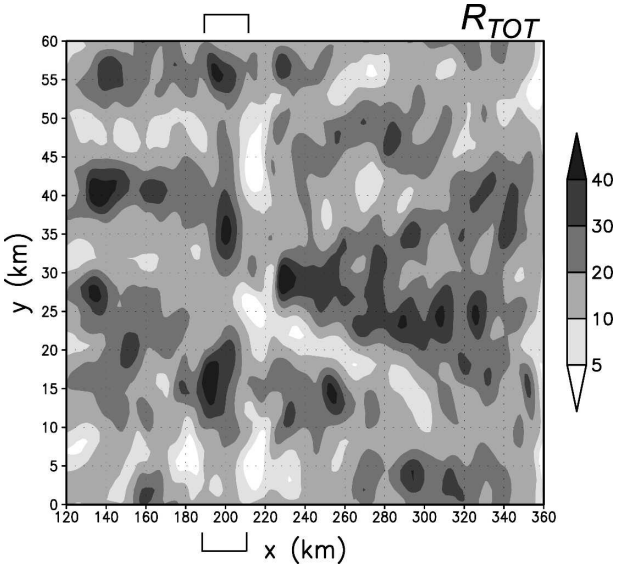

FIG. 25. As in Fig. 5 but for the H_0 = 600 m, x_{rm} = 10 km mountain ridge simulation. Brackets indicate the location of the mountain ridge.

weakening, and subsequent restrengthening as they traverse sinusoidal mountain ridges. If the terrain is high enough, discrete propagation occurs. Although this is only a pilot study, using highly idealized terrain configurations and physical parameterizations, it is our hope that these results will serve as a guide to the operational community and perhaps motivate additional studies of the interaction between convection and terrain. Following is a brief summary of results gleaned from the simulations.

Both the updrafts within and the precipitation field associated with a squall line are enhanced as a squall line moves up a slope. This enhancement is due to simple orographic ascent and occurs mainly within the system (i.e., is a result of parcel ascent behind the gust front rather than in front of it). In other words, the upslope flow does not act to trigger new cells, but, rather, to enhance existing ones, which are found behind the gust front because of their system-relative rearward propagation (cf. Figs. 28a and 28b). In the case of a longer slope, the enhancement persists for a

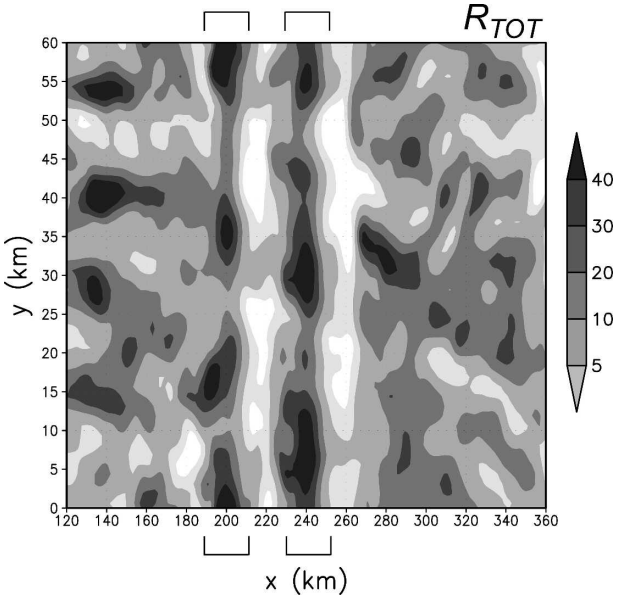

FIG. 26. As in Fig. 5 but for the two-ridge simulation with H_0 = 900 m and x_{rm} = 10 km. Brackets indicate the location of the mountain ridges.

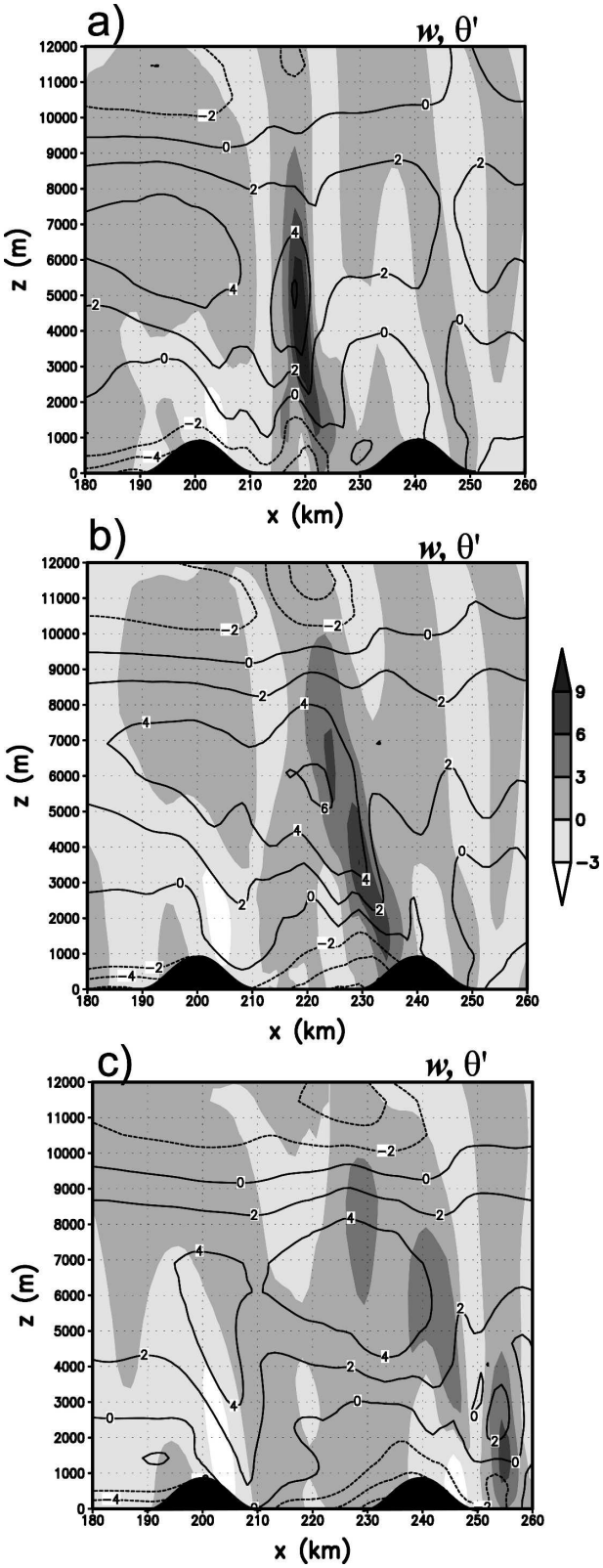

FIG. 27. As in Fig. 6 but for the two-ridge simulation with H_0 = 900 m and x_{rm} = 10 km for (a) 10 800, (b) 11 400, and (c) 12 000 s.

greater period of time. Steep slopes act as a strong quasi-two-dimensional forcing, helping to remove along-line variability within the system. Gradual slopes, however, allow such variability to persist.

A mountain of sufficient height can block a significant portion of the low-level cold outflow, reducing the amount of cold air on the lee side of the ridge. If enough cold air is blocked, the flow in the cold pool becomes so shallow that it transitions to supercritical as it descends the ridge. This leads to less lift at the front of the system and the formation of fewer and weaker cells. The sparseness of deep moist convection during descent creates a rain shadow over the lee slopes of the mountain. Cold outflow accumulates at the bottom of the slope, transitioning the flow in the cold pool back to subcritical, thereby forming a hydraulic jump. This hydraulic jump enables intense upward motion along the leading edge of the cold pool, resulting in the rapid generation of a new convective line (Fig. 28c).

A wide ridge allows for more gradual intensity fluctuations than does a steep ridge. A squall line weakens more as it traverses a higher ridge because more cold air is blocked by the mountain, resulting in less cold air and thus less lift at the gust front on the lee side of the ridge. The topography must have a height of 600–700 m in order for enough cold air to be blocked to cause discrete propagation. We suspect that this critical topography height varies from case to case, depending on environmental conditions, as they dictate important squall-line characteristics (e.g., height of the rear-inflow jet, and depth of and temperature deficit within the outflow). Also, multiple ridges influence the squall line in a manner nearly identical to an isolated ridge.

The propensity for damaging winds increases immediately downstream from a ridge and on the tops of high ridges. There is also a heightened risk of heavy rainfall as convection traverses steep terrain.

It is encouraging that some of the behavior seen in the Teng et al. (2000) study is replicated in this numerical study, such as a pronounced weakening of the squall line as it passes over high topography. In contrast to the Teng et al. study, however, the squall lines examined herein do not dissipate completely as they traverse a ridge, but they can pass over ridges and reintensify upon reaching their lee side. The maximum height of the terrain was significantly higher in the Teng et al. case, however. It is also possible that the environmental conditions over the higher terrain were unfavorable for the continuation of deep, moist convection in that case. In fact, additional simulations have been conducted (not shown) in which squall lines ascend slopes onto plateaus, and in those cases, it is nearly impossible to

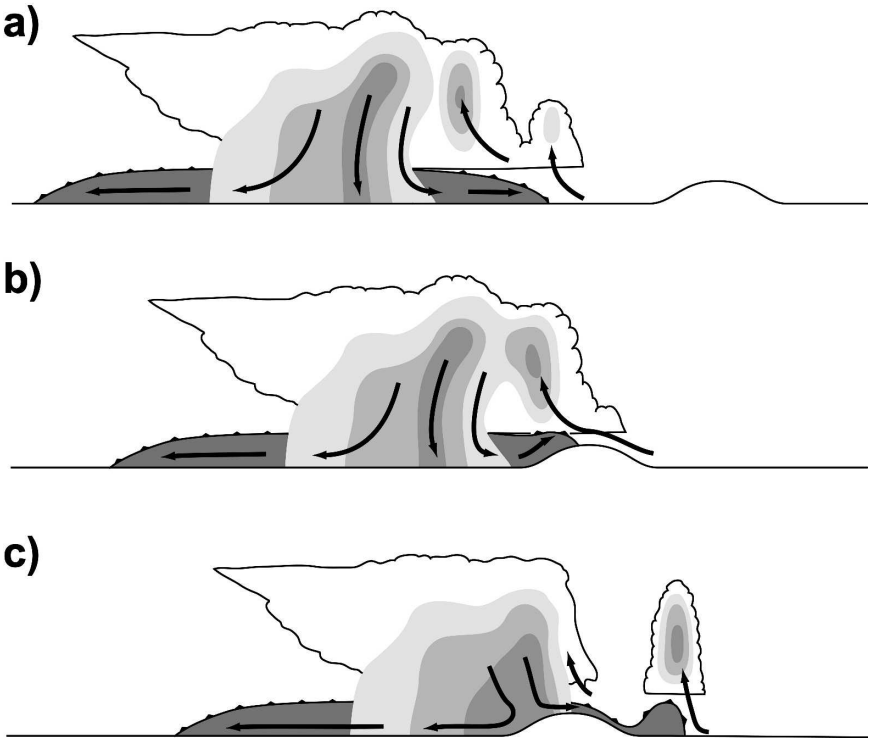

FIG. 28. (a) Schematic diagram of a steady-state squall line before any terrain interaction. The cloud outline is shown, shading indicates rainwater field, and the darkest shading indicates the cold pool. The gust front is marked by a bold line with triangles. Arrows denote system-relative airflow. (b) As in (a) but for a squall line ascending a ridge. The orographic ascent within the cold pool is shown. (c) As in (a) except for a squall line descending a ridge. Some of the cold air is blocked by the ridge. A hydraulic jump exists at the bottom of the slope, resulting in enhanced lift at the gust front and the generation of a new convective line as the original line weakens.

separate the effects of the changing environmental conditions from those of the terrain.

There is still a considerable amount of work to be done regarding the interaction between preexisting convection and terrain. Additional observational studies of convection traversing terrain features could confirm many of the conclusions reached from these idealized simulations. Also, more simulations are necessary to determine how environmental conditions influence the squall-line–terrain interactions reported here. For example, how sensitive are the results to the height of the RTF jet? How does a translation of the hodograph, which does not change the shear or system-relative winds but does change the mountain-relative winds, alter this evolution? Simulations using surface physics, higher grid resolution, and more realistic terrain configurations and microphysics schemes also should be attempted. Additionally, it would be helpful to investigate whether the response of the squall line to the terrain depends in any way on the evolutionary stage of the squall line. Finally, a study of how other convective modes (e.g., multicellular thunderstorm clusters and supercells) interact with terrain would complement these results. Terrain likely has different effects on other types of convective storms because of the vastly different circulation patterns within them.

Acknowledgments. Insightful comments from Drs. Yvette Richardson, John Clark, and three anonymous reviewers improved both the ideas expressed herein and the manuscript itself. This work was supported by a grant from the Cooperative Program for Operational Meteorology, Education and Training (COMET) Outreach Program (University Corporation for Atmospheric Research Award NA97WD0082). Part of this work was also supported by an American Meteorological Society graduate fellowship, sponsored by the National Weather Service. All plots were generated using the Grid Analysis and Display System (GrADS), developed by the Center for Ocean–Land–Atmosphere Studies at the Institute of Global Environment and Society.

REFERENCES

Adlerman, E. J., and K. K. Droegemeier, 2002: The sensitivity of numerically simulated mesocyclogenesis to variations in model physical and computational parameters. *Mon. Wea. Rev.,* **130,** 2671–2691.

Arya, S. P., 1988: *Introduction to Micrometeorology.* Academic Press, 307 pp.

Bischoff-Gauss, I., B. D. Gross, and F. Wipperman, 1989: Numerical studies on cold fronts. Part II: Orographic effects on gravity flows. *Meteor. Atmos. Phys.,* **40,** 159–169.

Braun, S. A., and R. A. Houze Jr., 1994: The transition zone and secondary maximum of radar reflectivity behind a midlatitude squall line. *J. Atmos. Sci.,* **51,** 2733–2755.

Bryan, G. H., J. C. Wyngaard, and J. M. Fritsch, 2003: Resolution requirements for the simulation of deep moist convection. *Mon. Wea. Rev.,* **131,** 2394–2416.

Chen, C., C. H. Bishop, G. S. Lai, and W.-K. Tao, 1997: Numerical simulations of an observed narrow cold-frontal rain band. *Mon. Wea. Rev.,* **125,** 1027–1045.

Chu, C.-M., and Y.-L. Lin, 2000: Effects of orography on the generation and propagation of mesoscale convective systems in a two-dimensional conditionally unstable flow. *J. Atmos. Sci.,* **57,** 3817–3837.

Coniglio, M. C., and D. J. Stensrud, 2001: Simulation of a progressive derecho using composite initial conditions. *Mon. Wea. Rev.,* **129,** 1593–1616.

Dudhia, J., 1993: A nonhydrostatic version of the Penn State–NCAR Mesoscale Model: Validation tests and simulation of an Atlantic cyclone and cold front. *Mon. Wea. Rev.,* **121,** 1493–1513.

Durran, D. R., and J. B. Klemp, 1982: On the effects of moisture on the Brunt–Vaisala frequency. *J. Atmos. Sci.,* **39,** 2152–2158.

Fovell, R. G., and Y. Ogura, 1988: Numerical simulation of a midlatitude squall line in two dimensions. *J. Atmos. Sci.,* **45,** 3846–3879.

——, and P.-H. Tan, 1998: The temporal behavior of numerically simulated multicell-type storms. Part II: The convective cell life cycle and cell regeneration. *Mon. Wea. Rev.,* **126,** 551–577.

Grady, R. L., and J. Verlinde, 1997: Triple-Doppler analysis of a discretely propagating, long-lived, high plains squall line. *J. Atmos. Sci.,* **54,** 2729–2748.

Houze, R. A., Jr., 2004: Mesoscale convective systems. *Rev. Geophys.,* **42,** RG4003, doi:10.1029/2004RG000150.

Karyampudi, V. M., S. E. Koch, C. Chen, J. W. Rottman, and M. L. Kaplan, 1995: The influence of the Rocky Mountains on the 13–14 April 1986 severe weather outbreak. Part II: Evolution of a prefrontal bore and its role in triggering a squall line. *Mon. Wea. Rev.,* **123,** 1423–1446.

Kessler, E., 1969: *On the Distribution and Continuity of Water Substance in Atmospheric Circulations. Meteor. Monogr.,* No. 32, Amer. Meteor. Soc., 84 pp.

Klemp, J. B., and R. B. Wilhelmson, 1978: The simulation of three-dimensional convective storm dynamics. *J. Atmos. Sci.,* **35,** 1070–1096.

Koch, S. E., 1999: Comments on "Numerical simulations of an observed narrow cold-frontal rainband." *Mon. Wea. Rev.,* **127,** 252–257.

——, and P. J. Kocin, 1991: Frontal contraction process leading to the formation of an intense narrow rainband. *Meteor. Atmos. Phys.,* **46,** 123–154.

Kundu, P. K., and I. M. Cohen, 2002: *Fluid Mechanics.* Academic Press, 759 pp.

Kuo, Y.-H., and G. T.-J. Chen, 1990: The Taiwan Area Mesoscale Experiment (TAMEX): An overview. *Bull. Amer. Meteor. Soc.,* **71,** 488–503.

Lin, Y.-L., and L. E. Joyce, 2001: A further study of mechanisms of cell regeneration, development, and propagation within two-dimensional multicell storms. *J. Atmos. Sci.,* **58,** 2957–2988.

——, R. L. Deal, and M. S. Kulie, 1998: Mechanisms of cell regeneration, development, and propagation within a two-dimensional multicell storm. *J. Atmos. Sci.,* **55,** 1867–1886.

Mahrer, Y., 1984: An improved numerical approximation of the horizontal gradients in a terrain-following coordinate system. *Mon. Wea. Rev.,* **112,** 918–922.

Moncrieff, M. W., and M. J. Miller, 1976: The dynamics and simulation of a tropical squall line. *Quart. J. Roy. Meteor. Soc.,* **102,** 372–394.

Newton, C. W., 1950: Structure and mechanism of the prefrontal squall line. *J. Meteor.,* **7,** 210–222.

Raymond, D., and M. Wilkening, 1980: Mountain-induced convection under fair weather conditions. *J. Atmos. Sci.,* **37,** 2693–2706.

Rotunno, R., J. B. Klemp, and M. L. Weisman, 1988: A theory for strong, long-lived squall lines. *J. Atmos. Sci.,* **45,** 463–485.

Smith, R. B., 1979: The influence of mountains on the atmosphere. *Advances in Geophysics,* Vol. 21, Academic Press, 87–230.

Smull, B. F., and R. A. Houze Jr., 1985: A midlatitude squall line with a trailing region of stratiform rain: Radar and satellite observations. *Mon. Wea. Rev.,* **113,** 117–133.

——, and ——, 1987: Rear inflow in squall lines with trailing stratiform precipitation. *Mon. Wea. Rev.,* **115,** 2869–2889.

Teng, J.-H., C.-S. Chen, T.-C. C. Wang, and Y.-L. Chen, 2000: Orographic effects on a squall line system over Taiwan. *Mon. Wea. Rev.,* **128,** 1123–1138.

Weisman, M. L., 1992: The role of convectively generated rear-inflow jets in the evolution of long-lived mesoconvective systems. *J. Atmos. Sci.,* **49,** 1826–1847.

——, 1993: The genesis of severe, long-lived bow echoes. *J. Atmos. Sci.,* **50,** 645–670.

——, and J. B. Klemp, 1982: The dependence of numerically simulated convective storms on vertical wind shear and buoyancy. *Mon. Wea. Rev.,* **110,** 504–520.

——, ——, and R. Rotunno, 1988: Structure and evolution of numerically simulated squall lines. *J. Atmos. Sci.,* **45,** 1990–2013.

Williams, R. T., M. S. Peng, and D. A. Zankofski, 1992: Effects of topography on fronts. *J. Atmos. Sci.,* **49,** 287–305.

Xu, Q., M. Xue, and K. K. Droegemeier, 1996: Numerical simulations of density currents in sheared environments within a vertically confined channel. *J. Atmos. Sci.,* **53,** 770–786.

Xue, M., K. K. Droegemeier, and V. Wong, 2000: The Advanced Regional Prediction System (ARPS): A multiscale nonhydrostatic atmospheric simulation and prediction tool. Part I: Model dynamics and verification. *Meteor. Atmos. Phys.,* **75,** 161–193.

——, and Coauthors, 2001: The Advanced Regional Prediction System (ARPS): A multiscale nonhydrostatic atmospheric simulation and prediction tool. Part II: Model physics and applications. *Meteor. Atmos. Phys.,* **76,** 143–165.

Yang, M.-J., and R. A. Houze Jr., 1995: Sensitivity of squall-line rear inflow to ice microphysics and environmental humidity. *Mon. Wea. Rev.,* **123,** 3175–3193.